Available online at www.sciencedirect.com

ScienceDirect

Geochimica et Cosmochimica Acta 138 (2014) 1–20

Geochimica et Cosmochimica Acta

www.elsevier.com/locate/gca

Hydromagnesite solubility product and growth kinetics in aqueous solution from 25 to 75 °C

Quentin Gautier [a,b,*], Pascale Bénézeth [a], Vasileios Mavromatis [a], Jacques Schott [a]

[a] Géosciences Environnement Toulouse (GET), Observatoire Midi-Pyrénées, Université de Toulouse, CNRS, IRD, 14, avenue Edouard Belin, F-31400 Toulouse, France

[b] Université Paris-Est, Laboratoire Navier, 6/8 avenue Blaise Pascal, Champs-sur-Marne, 77455 Marne-La-Vallée, France

Received 11 November 2013; accepted in revised form 30 March 2014; available online 13 April 2014

Abstract

Hydromagnesite $Mg_5(CO_3)_4(OH)_2{\cdot}4H_2O$ is the most widespread form of hydrated Mg-carbonate minerals. To better understand the factors controlling the precipitation of hydrated Mg-carbonates, we measured hydromagnesite solubility product at 25 and 50 °C and its growth rate between 25 and 75 °C, using natural hydromagnesite from a cave as seed material.

The solubility products values derived in this study, $K_{sp-Hmgs} = -37.08 \pm 0.50$ and -38.90 ± 0.54 at 25 and 50 °C, respectively, are in the upper range of published values. Hydromagnesite growth rate normalized to the BET surface area at $8 \leqslant pH \leqslant 10$ is consistent with the direct and reversible attachment of the reactants at the solid surface being rate-limiting. It may be described by:

$$R_{Hmgs} = A_0 \cdot e^{-Ea/RT}(\Omega_{Hmgs}^{1/5} - 1)$$

where A_0, the pre-exponential factor, and Ea, the activation energy, are equal to 5.12×10^{-7} mol/cm^2/s and 45.5 ± 9 kJ/mol, respectively, and Ω_{Hmgs} stands for the saturation state of the solution with respect to hydromagnesite. Comparison of hydromagnesite growth rates with recently published magnesite growth rates (Saldi et al., 2009, 2012) show that: (1) hydromagnesite apparent growth activation energy is lower by more than 100 kJ/mol compared to the activation energy for magnesite obtuse step advancement, and (2) hydromagnesite growth rate constant extrapolated to 90 °C is 2.5 orders of magnitude higher than corresponding magnesite growth rate constant. Thus, our results confirm the long-standing hypothesis that the slow dehydration kinetics of the Mg^{2+} cation is responsible for the sluggish magnesite formation at low temperature, and that the kinetic barrier for hydromagnesite growth is much lower. Nevertheless, simulation of hydromagnesite and magnesite growth rates as a function of solution composition at 50 and 90 °C, and pH 7 and 9 reveal that, because of its much higher solubility, hydromagnesite would grow more quickly than magnesite in natural or industrial environments only at 50 °C and pH 9. This is consistent with the formation of hydromagnesite during the surface alteration of ultramafic rocks.
© 2014 Elsevier Ltd. All rights reserved.

1. INTRODUCTION

Magnesite is the most stable Mg-carbonate mineral in a wide range of temperatures (Königsberger et al., 1999; Bénézeth et al., 2011). However, despite its structural, chemical and thermodynamic similarity with calcite, the mineral is well known for its reluctance to form at ambient temperature. Indeed, direct magnesite precipitation from

* Corresponding author. Present address: Ministère de l'Ecologie, du Développement Durable et de l'Energie, Tour Voltaire, 1, place des Degrés, 92055 La Défense cedex, France. Tel.: +33 678983195.

E-mail address: quentin.gautier@normalesup.org (Q. Gautier).

http://dx.doi.org/10.1016/j.gca.2014.03.044
0016-7037/© 2014 Elsevier Ltd. All rights reserved.

aqueous solution has been observed only at temperatures higher than ca. 60–80 °C (e.g. Usdowski, 1989; Hänchen et al., 2008; Saldi et al., 2009, 2012), while at lower temperatures, its formation during forsterite carbonation requires the presence of water-saturated supercritical CO_2 (Felmy et al., 2012; Bénézeth et al., 2013; Schaef et al., 2013). This reluctance to form is interpreted to stem from a kinetic inhibition, which is widely ascribed to the highly hydrated character of the Mg^{2+} cation (Lippmann, 1973; Sayles and Fyfe, 1973) and resulting low water exchange rate between Mg^{2+} first hydration shell and the bulk of the solution (Bleuzen et al., 1997).

At temperatures lower than 60–80 °C, Mg-carbonates tend to precipitate under the form of various hydrated compounds, depending on solution composition and temperature (see Hopkinson et al., 2012, and references therein). At temperatures higher than 15 °C, hydromagnesite $Mg_5(CO_3)_4(OH)_2{\cdot}4H_2O$ is the second most stable Mg-carbonate mineral, followed by nesquehonite $MgCO_3{\cdot}3H_2O$ (Königsberger et al., 1999; Marion, 2001). Both minerals may form at ambient temperature (Hänchen et al., 2008; Hopkinson et al., 2012), although it is generally reported that nesquehonite is more readily formed at 25 °C, particularly under relatively high CO_2 pressures, while hydromagnesite is obtained at relatively higher temperatures (Hänchen et al., 2008; Wang et al., 2008; Cheng et al., 2009; Cheng and Li, 2010a,b). In addition, artinite $Mg_2(CO_3)(OH)_2{\cdot}3H_2O$ may become more stable than hydromagnesite at temperatures lower than 15 °C and low pCO_2 (Königsberger et al., 1999), while lansfordite $MgCO_3{\cdot}5H_2O$ may form at the expense of nesquehonite at temperatures lower than ca. 10 °C (Marion, 2001).

Mineralogical transitions readily occur between the different Mg-carbonate phases. Nesquehonite is known to transform into hydromagnesite via the intermediate formation of dypingite $Mg_5(CO_3)_4(OH)_2{\cdot}5H_2O$ (Davies and Bubela, 1973; Hopkinson et al., 2008, 2012), while a transition between hydromagnesite and magnesite was documented above 100 °C by Sayles and Fyfe (1973), Zhang et al. (2000) and Hänchen et al. (2008). Furthermore, magnesite formation at temperatures as low as 35 °C seems to be facilitated by the transformation of an initially formed nesquehonite phase (Schaef et al., 2011; Felmy et al., 2012).

Hydrated Mg-carbonate minerals are relatively common in natural environments, where they are encountered as weathering products of mafic or ultramafic rocks such as serpentinite or basalt (see Deelman, 2011 and references therein) or precipitates in evaporitic environments (Alderman and Von der Borch, 1960; Von der Borch, 1965; Goto et al., 2003). Hydromagnesite is commonly found in calcareous or dolomitic caves, within speleothems or forming on top of aragonite concretions or as a component of "moonmilk" (Fischbeck and Müller, 1971; Thrailkill 1971; Northup et al., 2001). It is believed to form from Mg-rich waters that have seeped through the sedimentary rock. Hydromagnesite also presents a particular interest as a biomineral: it has been found to precipitate in microbial mats or stromatolites in a number of alkaline lakes such as Salda Lake in Turkey, British Columbia lakes or Alchichica Lake in Mexico (Thompson and Ferris, 1990; Renault and Stead, 1990; Braithwaite and Zedef, 1996; Russell et al., 1999; Power et al., 2007; Kazmierczak et al., 2011; Mavromatis et al., 2012,2013; Shirokova et al., 2013). Overall, environments were hydromagnesite currently forms are characterized by high pH and high Mg/Ca ratio.

Hydromagnesite and nesquehonite have recently attracted a great deal of interest for their potential capacity to store CO_2 under a mineral form, particularly at low temperature where magnesite does not form. Experimental studies have addressed the formation conditions of different hydrated Mg-carbonate minerals (Hänchen et al., 2008) as well as their thermal stability (Frost et al., 2008; Ballirano et al., 2010), while others aimed at precipitating hydromagnesite or nesquehonite as a result of low temperature carbonation of serpentine (Park and Fan, 2004; Teir et al., 2007, 2009) or brucite (Zhao et al., 2009; Schaef et al., 2011; Loring et al., 2012). Besides, field studies have proven passive CO_2 sequestration in ultramafic mine tailings through the weathering of Mg-silicates and precipitation of hydrated Mg-carbonates, including hydromagnesite (Wilson et al., 2009; Pronost et al., 2011). Similarly, Power et al. (2009) proposed hydromagnesite bio-mediated precipitation in lakes of British Columbia as a biogeochemical model for CO_2 sequestration at the watershed scale.

Thus, there is a wide interest in better understanding the formation and the evolution of hydrated Mg-carbonate minerals. No study has yet investigated in detail the kinetics of formation of hydrated Mg-carbonates, as compared to their anhydrous counterpart. This information, however, is essential both for the fundamental understanding of the role of Mg^{2+} hydration on the formation of various Mg-carbonate phases, and in order to better quantify and optimize the potential role of hydrated Mg-carbonates in low- and high-temperature CO_2 sequestration.

The present study focuses on hydromagnesite, the most widespread Mg-carbonate mineral forming in the Earth's surface environments. Considering the important variability of published measurements of hydromagnesite solubility product (e.g. Langmuir, 1965; Königsberger et al., 1999), we first determined directly the solubility product of our seed material, a natural hydromagnesite retrieved from caves in the French Pyrénées Orientales, at 25 and 50 °C. We then measured its growth rates under controlled conditions of supersaturation at temperatures from 25 to 75 °C. The existence of published data on magnesite growth kinetics (Saldi et al., 2009, 2012; Gautier, 2012) allows for an insightful comparison between these two magnesium carbonates of different hydration state.

2. THEORETICAL CONSIDERATIONS

Hydromagnesite dissolution and precipitation in aqueous solution can be described by the following reaction:

$$Mg_5(CO_3)_4(OH)_2 \cdot 4H_2O_{(s)} = 4\,CO_3^{2-} + 5\,Mg^{2+} + 2\,OH^- + 4\,H_2O \quad (1)$$

Hydromagnesite solubility product is defined as the equilibrium constant of reaction (1):

$$K_{sp\text{–}Hmgs} = a^5_{Mg^{2+}} \cdot a^4_{CO_3^{2-}} \cdot a^2_{OH^-} \cdot a^4_{H_2O} \quad (2)$$

where a_i is the chemical activity of the ith species at equilibrium.

The apparent equilibrium constant of reaction (1) is defined as:

$$Q_{sp\text{–}Hmgs} = m^5_{Mg^{2+}} \cdot m^4_{CO_3^{2-}} \cdot m^2_{OH^-} \quad (3)$$

The solubility product $K_{sp\text{–}Hmgs}$ can thus be calculated from:

$$K_{sp\text{–}Hmgs} = Q_{sp\text{–}Hmgs} \cdot \gamma^5_{Mg^{2+}} \cdot \gamma^4_{CO_3^{2-}} \cdot \gamma^2_{OH^-} \cdot a^4_{H_2O} \quad (4)$$

where γ_i corresponds to the activity coefficient of the ith species, and a_{H_2O} is the chemical activity of water.

The saturation state of solutions with respect to hydromagnesite is defined in the given experimental conditions as:

$$\Omega_{Hmgs} = \frac{a^5_{Mg^{2+}} \cdot a^4_{CO_3^{2-}} \cdot a^2_{OH^-} \cdot a^4_{H_2O}}{K_{sp\text{–}Hmgs}} \quad (5)$$

The standard state adopted in this study is that of unit activity for pure minerals and H_2O at any temperature and pressure. For dissolved species the standard state is of unit activity in a hypothetical 1 molal solution referenced to infinite dilution at any temperature and pressure. Aqueous solution speciation, saturation states with respect to solid phases, and solution pH at temperatures higher than 25 °C were calculated from measured Mg concentration, alkalinity, and pH measured at room temperature, using the PHREEQC geochemical code (Parkhurst and Appelo, 1999) together with its llnl.dat thermodynamic database. The latter was modified to include the carbonic acid dissociation constants of Millero et al. (2007), the thermodynamic constant for Mg^{2+} hydrolysis (Palmer and Wesolowski, 1997), and the newly measured hydromagnesite solubility product from this study (see Section 4.1), while the activity model used to compute activity coefficients is the Davies model. The Davies equation is valid up to ionic strengths of 0.1 M. In the range of ionic strengths investigated in our solubility and growth experiments, it was verified that the chemical speciation calculation using the mean stoichiometric activity coefficient approach of Lindsay, 1989, gives the same results, within uncertainties, as those obtained with the Davies equation.

Mineral dissolution and growth rates are commonly described using (Lasaga, 1995; Schott et al., 2012):

$$R = k \cdot e^{-\frac{E_a}{RT}} \left[\prod_i a_i^{m_i}\right] f(\Delta G) \quad (6)$$

where k is a rate constant, E_a represents the apparent activation energy of the overall reaction, a_i and m_i refer respectively to the activity of the ith species involved in the reaction mechanism and to the reaction order with respect to this species, and the last term $f(\Delta G)$ accounts for the variation of the rate with the deviation from equilibrium. The analysis of crystal growth kinetics within the framework of transition state theory (TST) and the classical crystal growth theory suggests that $f(\Delta G)$ can be expressed as $f(\Delta G) = (e^{\Delta G/\sigma RT} - 1)^n$. In this expression n represents the order of the rate dependence on ΔG and σ stands for the Temkin's average stoichiometric number (Temkin, 1963). Within TST, σ is equal to the ratio of the rate of destruction of the activated complex controlling the growth reaction with respect to the overall reaction rate (Aagaard and Helgeson, 1982; Schott et al., 2009). Incorporating in Eq. (6) the expression of $f(\Delta G)$ and substituting $\Omega = e^{\Delta G/RT}$, the solution saturation state with respect to the growing solid, yields the following expression of the growth rate:

$$R = k_{(+)} \left[\prod_i a_i^{m_i}\right] (\Omega^{1/\sigma} - 1)^n \quad (7)$$

where $k_{(+)}$ is the surface area normalized growth rate constant at a given temperature.

It should be underlined that TST applies to single elementary reactions, whereas hydromagnesite formation is most likely a complex multi-steps mechanism. However, considering that the dehydration at the solid-solution interface of the strongly hydrated Mg^{2+} cation has been suggested to control Mg-carbonate minerals overall growth kinetics (Lippmann, 1973; Pokrovsky and Schott, 2002; Saldi et al., 2009; Schott et al., 2009), we hypothesize that the rate-controlling step for hydromagnesite growth is the Mg^{2+} aquo ion partial dehydration, and that the corresponding activated complex contains one Mg^{2+}. Thus for hydromagnesite which contains five Mg, $\sigma = 5$, and Eq. (7) may be written in a simplified form:

$$R = k_{Hmgs}(\Omega^{1/5}_{Hmgs} - 1)^n \quad (8)$$

where the apparent growth rate constant k_{Hmgs} contains information concerning the dependency of growth rates with respect to solution chemistry.

The parameter n has classically been related to the type of growth-controlling mechanism: $n = 1$ for transport or adsorption controlled growth, $n = 2$ for spiral growth at screw dislocations, while higher orders reveal 2D nucleation-assisted growth (e.g. Nielsen, 1984; Blum and Lasaga, 1987; Shiraki and Brantley, 1995). Thus, fitting Eq. (8) to our experimentally determined hydromagnesite precipitation rates should provide information regarding the growth-controlling mechanism in our experimental conditions.

3. MATERIALS AND METHODS

3.1. Hydromagnesite seeds

Solubility and precipitation experiments were performed on the same pure natural hydromagnesite originating from the André Lachambre cave network, in the French Pyrénées Orientales. This karstic network set in a calcareous massif of Devonian age is well known for numerous aragonite and hydromagnesite concretions. Hydromagnesite occurs as small aggregates growing on aragonite needles. It likely forms from a Mg-rich and Ca-depleted fluid that has seeped through the caprock and has already precipitated aragonite.

Scanning electron microscope (SEM) observations of the centimeter-sized hydromagnesite "flowers" revealed

agglomerates of rectangular to elongated hexagonal-shaped crystals, up to 80 μm long, 60 μm wide, and 2 μm thick (Fig. 1a). In order to disaggregate hydromagnesite agglomerates, the natural samples were gently grounded in an agate mortar, thus producing a finely divided seed material (Fig. 1b), which was used without modification for experiments. The results of electron microprobe analyses performed on hydromagnesite crystals are shown in Table 1, and indicate only minor amounts of impurities. The diffractogram of the grinded material provided in Fig. 2, performed on an INEL CPS 120 diffractometer using the Co Kα ray, confirmed the sample was pure hydromagnesite.

The exact stoichiometry of hydromagnesite has been under debate over the last decades, as to whether its structural formula contained 3 or 4 water molecules (for a review of the controversy, see Hollingbery and Hull, 2010b). However, there seems to be now an agreement on the formula: $Mg_5(CO_3)_4(OH)_2{\cdot}4H_2O$. The thermo-gravimetric analyses (TGA) performed on the hydromagnesite crystals used in this study correspond to this formula (see detailed results in Appendix A).

The specific BET surface area of hydromagnesite powders was determined by multi-point nitrogen adsorption using an Autosorb 1 (Quantachrome Instruments). Degassing of the samples prior to gas adsorption has been performed at temperatures lower than 90 °C so as to not dehydrate the mineral. The measured specific surface area is 3.56 $m^2/g \pm 5\%$ (mean of 3 measurements).

3.2. Hydromagnesite solubility experiments

Solubility experiments were performed at 25 and 50 °C in 250 mL Azlon® polypropylene beakers capped with a tight home-made polypropylene cap and sealed with an O-ring, and placed in thermostated baths maintaining the temperature to within 0.5 °C of the reaction temperature. At 25 °C, 0.5 g of hydromagnesite powder was placed in three different beakers filled with approximately 220 mL of (1) 0.1 M NaCl solution, (2) 0.01 M NaCl solution, and (3) high purity deionized water (resistivity 18.2 MΩ). At 50 °C, two experiments were performed with 0.4 g of powder in either (1) 0.1 M NaCl solution or (2) 0.01 M NaCl solution. The filling solution was heated to the experimental temperature in the beaker prior to hydromagnesite seeds addition. Solutions were stirred by Teflon-coated floating magnetic bars to limit powder grinding.

The caps had an aperture closed by a Teflon-coated silicon septum maintained with a stainless steel pierced screw allowing fluid sampling. Solution samples (approximately 6 mL) were regularly withdrawn using polypropylene syringes and filtered through 0.22 μm Millipore Nylon filters. 2 mL of solution were stored at 4 °C for subsequent alkalinity measurements. A small aliquot was used for immediate pH measurement, and the rest of the sample was acidified

Table 1
Chemical composition of the Lachambre hydromagnesite used in this study, based on 15 EMPA analyses. Note the good agreement between the measured total weight percent of carbonate oxides, and the theoretical value corresponding to hydromagnesite stoichiometry (43.09 %).

Major oxides	(wt.%)
MgO	42.79
CaO	0.04
MnO	0.03
FeO	0.03
SrO	0.01
BaO	–
sum	42.90
SiO_2	0.07

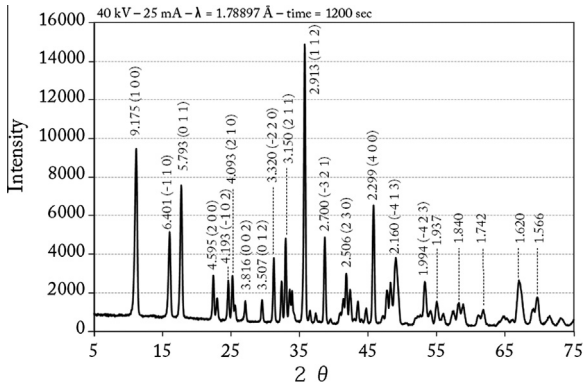


Fig. 2. Diffractogram of the powdered seed material with crystallographic indexation of the main peaks. All peaks correspond to hydromagnesite.

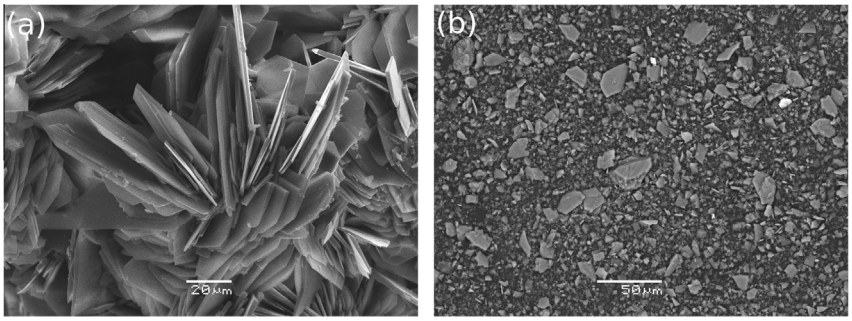


Fig. 1. SEM pictures of hydromagnesite seeds and precipitates. (a) Secondary electron (SE) image of a pristine hydromagnesite "flower" from the Lachambre cave network. (b) Backscattered electron (BSE) image of highly divided hydromagnesite fragments obtained after gentle grinding, and used for solubility and growth experiments. Bright spots correspond to aragonite fragments.

for later Mg concentration analysis. At 50 °C, solution aliquots had to be cooled down to 25 °C in a thermostated water bath for pH measurement.

Solubility experiments lasted up to 60 days, during which pH and dissolved Mg concentration measurements allowed to follow the approach of equilibrium. At the end of the experiments, the solids were recovered, filtered through a 0.22 μm Millipore cellulose acetate filter using suction filtration, quickly rinsed with ultrapure deionized water and then frozen at −80 °C and freeze dried. This drying procedure was chosen so as to preserve the mineralogy of the final solids, since mineralogical transitions between various forms of hydrated Mg-carbonates are well documented, and occur quickly at temperatures of 60 °C or less (Davies and Bubela, 1973; Hopkinson et al., 2008). The final powders were examined with SEM and XRD, which revealed no visible difference compared to the initial material. We are thus confident that no other hydrated Mg-carbonate phases precipitated during the course of the experiments, and that measured solubility products are truly those of natural hydromagnesite.

3.3. Growth experiments

At 25 °C and 30 °C, growth experiments were conducted using a mixed-flow reactor experimental setup described in Mavromatis et al. (2013). A 1000 mL polypropylene reaction vessel is initially filled with 500 mL of solution close to equilibrium with hydromagnesite at pH 9.2 and an ionic strength of 0.11 M. The reactor is immersed in a thermostated bath and stirred by a magnetic stirrer at ~150 rpm. 0.8–1.5 g of grounded hydromagnesite seeds are introduced in the vessel and hydromagnesite precipitation is induced by pumping in the reactor two independent $MgCl_2{\cdot}6H_2O$ and Na_2CO_3 inlet solutions at similar and constant flow rates (9–12 mL/day) using a peristaltic pump (Fig. 3). In two experiments (H6 and H8, see Table 2) pCO_2 and pH were maintained constant through continuous bubbling of water-saturated air in the reactor (Fig. 3).

During the course of a run, introduction of inlet solutions causes the volume of the solution in the reactor to increase. Once a day, a volume equal to the volume of the inlet solutions added in 24 h is sampled from the reactors with a syringe, thus limiting the reactor solution volume variation to maximum 5% over a 24-h interval. This sampled solution is called thereafter "outlet solution".

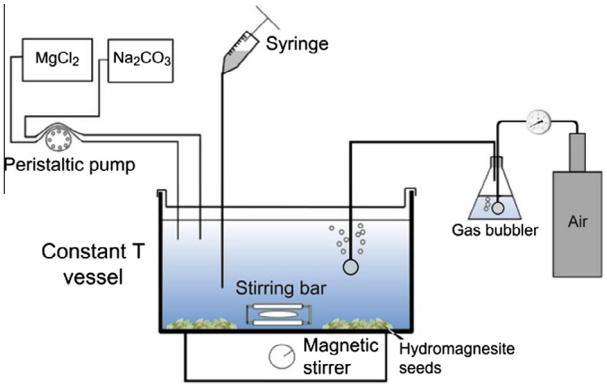


Fig. 3. Mixed-flow reactor setting used for low temperature hydromagnesite growth experiments. Note that air bubbling was only used in experiments H6 and H8 at 30 °C.

Immediately after sampling, samples were filtered through a 0.22 μm nylon Millipore filter, and precisely weighted. A sub-sample was used for pH measurement, another one acidified for subsequent Mg concentration analysis, while the remaining of the sample was stored at 4 °C for alkalinity measurement. At the end of the experiments, the solution and the solid in the reactor were separated by suction filtration through a 0.22 μm cellulose acetate Millipore filter. The solid was quickly rinsed with ultrapure deionized water, then frozen at −80 °C and freeze dried. Dried solids were examined by SEM and XRD. Over the course of the experiments, addition of inlet solutions increases reactor solution supersaturation with respect to hydromagnesite, which in turn increases the rate of mineral precipitation until steady-state growth conditions are established. Steady-state is reached when solution Mg concentration and pH remains constant within analytical uncertainties for a minimum of 6 consecutive days (corresponding to a 20% renewal of the solution volume), which took 30–35 days in our experiments. Growth rates at steady-state are classically estimated from the change of Mg concentration between the inlet solution and the sampled fluids:

$$R = \frac{FR_{tot}\Delta[\mathrm{Mg}]_{tot}}{5m_{Hmgs}S_{BET}} \quad (9)$$

where FR_{tot} represents the total inlet fluid flow rate (equal to the sum of the respective flow rates of each inlet solution), m_{Hmgs} the initial hydromagnesite seeds mass and S_{BET} the initial specific BET surface area. $\Delta[\mathrm{Mg}]_{tot}$ is the change of Mg concentration between the total inlet fluid and the outlet solution. The factor 5 takes into account hydromagnesite stoichiometry with respect to Mg.

In addition to steady-state rates, we calculated daily precipitation rates based on a precise Mg mass balance calculation. Namely, between time steps t_1 and t_2, corresponding to fluid sampling events, the variation of the number of moles of dissolved Mg in the reactor, $\Delta n_{\mathrm{Mg}(tot)}$, is equal to:

$$\Delta n_{\mathrm{Mg}(tot)} = n_{\mathrm{Mg}(added)} - n_{\mathrm{Mg}(sampled)} - n_{\mathrm{Mg}(pp)} \quad (10)$$

where $n_{\mathrm{Mg}(added)}$ is the amount of Mg added to the reactor by the inlet solution, $n_{\mathrm{Mg}(sampled)}$ is the amount of Mg withdrawn from the reactor at t_2, and $n_{\mathrm{Mg}(pp)}$ is the amount of Mg precipitated in the reactor between t_1 and t_2. $n_{\mathrm{Mg}(added)}$ is quantified from the inlet Mg concentration and flow rate, and $n_{\mathrm{Mg}(sampled)}$ from the volume of sampled solution and its Mg concentration. $\Delta n_{\mathrm{Mg}(tot)}$ can be easily calculated from the volume of the reactor solution and its Mg concentration at t_1 and at t_2. The hydromagnesite precipitation rate between t_1 and t_2 (thereafter called "daily precipitation rate") can thus be estimated from:

$$R_{\mathrm{daily}} = n_{\mathrm{Mg}(pp)}/(5\cdot(t_2 - t_1)\cdot m_{Hmgs}\cdot S_{BET}) \quad (11)$$

Overall uncertainties reach at least 30% of the calculated rates due to the small daily variations of Mg concentration and slight variations of inlet flow rates during

Table 2
Inlet solution composition for 25 and 30 °C hydromagnesite growth experiments. For each experiment, the composition of the two independent inlet solutions is reported. "slt" stands for "solution", "FR" for "flow rate".

Solution	T (°C)	Exp. Type		$MgCl_2$ (mol/kgw)	Na_2CO_3 (mol/kgw)	NaCl (mol/kgw)	FR (mL/h) Mg slt.	FR (mL/h) CO_3 slt.
H9	25	No air bubbling	Slt. 1	2.60×10^{-2}		0.037	0.356	
			Slt. 2		2.00×10^{-2}	0.056		0.358
H10	25	No air bubbling	Slt. 1	3.12×10^{-2}		0.022	0.382	
			Slt. 2		2.40×10^{-2}	0.045		0.380
H11	25	No air bubbling	Slt. 1	4.11×10^{-2}		–	0.351	
			Slt. 2		3.20×10^{-2}	0.030		0.337
H12	25	No air bubbling	Slt. 1	5.10×10^{-2}		–	0.370	
			Slt. 2		4.00×10^{-2}	0.038		0.372
H6	30	Air bubbling	Slt. 1	3.37×10^{-2}		0.022	0.537	
			Slt. 2		2.40×10^{-2}	0.045		0.519
H8	30	Air bubbling	Slt. 1	5.43×10^{-2}		–	0.499	
			Slt. 2		4.00×10^{-2}	0.038		0.505

the course of the experiments. Calculated daily precipitation rates were averaged over periods of 3 days, so as to smooth the variability introduced by slight analytical variations. Despite uncertainties, these daily rate calculations bring insights into the evolution of hydromagnesite precipitation rates as a function of saturation state during the course of a single experiment. Given the duration of the runs, the daily rates can be assumed to represent a steady growth mechanism at the mineral surface. Table 2 provides a list of all growth experiments performed at 25 °C and 30 °C.

At 50 and 75 °C, hydromagnesite growth experiments were performed with high temperature titanium mixed-flow reactors following the procedure described by Saldi et al. (2012). At the beginning of the experiment, ~1 g of mineral powder is placed at ambient temperature in the reactor filled with a solution close to equilibrium with hydromagnesite at the temperature and pH of interest. The reactor is then quickly sealed and heated to the desired temperature. A supersaturated inlet solution is injected into the reactor with an HPLC pump, at flow rates ranging from 0.25 to 2 mL/min. The outlet solution leaves the reactor through a 2 µm titanium frit, and is cooled down with a water refrigerating system before sampling. pH is measured at ambient temperature immediately after sampling. A sub-sample is stored at 4 °C for alkalinity measurement and another one is acidified and stored for subsequent Mg concentration measurement. Steady-state precipitation rates, indicated by a constant outlet Mg concentration over a minimum of three residence times, were calculated from the variation of Mg concentration between the inlet and the steady-state outlet fluid $\Delta[Mg]_{tot}$ using Eq. (9). Compared to the low temperature setting, this reactor allows for a more precise monitoring of the flow rate, which can be directly measured by weighing outlet fluid samples. In addition, saturation state can be simply changed by modifying inlet solution or flow rate. In the present case, experiments were run in series of different flow rates on the same seeds while keeping the same inlet solution composition. Table 3 provides a list of inlet solution compositions used for experiments performed at 50 and 75 °C.

3.4. Solution preparation and chemical analysis

All solutions were prepared from high purity deionized water (resistivity 18.2 MΩ), reagent grade NaCl, $MgCl_2 \cdot 6H_2O$, $NaHCO_3$ and high purity 1 M NaOH solutions. The NaCl concentration was adjusted to obtain an ionic strength close to 0.1 M in most experiments. Experiments were performed in alkaline conditions, with solution pH chosen so as to limit supersaturation with respect to brucite and nesquehonite. For titanium mixed-flow reactor experiments, the chemistry of inlet solutions was designed in order to obtain activity ratios $\frac{a_{Mg^{2+}}}{a_{CO_3^{2-}}}$ close to 1.25, corresponding to the magnesium to carbonate ratio of hydromagnesite structural formula. For low-temperature growth experiments, this control was less well achieved (see Tables 8 and 9).

Solution pH was measured with a standard Mettler Toledo glass electrode calibrated against NIST standard buffers (pH 4.01, 6.86, 9.18 at 25 °C), with an uncertainty of 0.02 units. For solubility and growth experiments, pH measurements were performed at ambient temperature and pH at the experimental temperature was recalculated with PHREEQC using the llnl.dat database.

Experimental solutions were analyzed for magnesium by flame atomic absorption spectroscopy using a Perkin Elmer AAnalyst 400 with an uncertainty of ±1% and a detection limit of 6×10^{-7} M. Alkalinity was measured by mean of automatic HCl titration on a Schott TitroLine Alpha Plus titrator, with an uncertainty of ±2% and a detection limit of 5×10^{-5} M.

4. RESULTS

4.1. Hydromagnesite solubility product

Progress of the dissolved Mg concentration throughout the course of the solubility experiments performed at 25 and 50 °C is presented in Fig. 4. Stable Mg concentrations are reached after approximately 1150 h at 25 °C, and solution composition measured in the last two samples of the experiments, reported in Table 4, was estimated to be

Table 3
Inlet solution composition for mixed-flow reactor experiments (MFR) performed at 50 and 75 °C.

Solution	T (°C)	Exp. Type	Filling slt.	Inlet pH (25 °C)	$MgCl_2$ (mol/kgw)	$NaHCO_3$ (mol/kgw)	NaCl (mol/kgw)	NaOH (mol/kgw)
H504B	50	MFR	mQ water	9.16	2.59×10^{-3}	1.06×10^{-2}	0.085	2.65×10^{-3}
H504C-D	50	MFR	equil. pH 9.45	9.44	2.62×10^{-3}	1.06×10^{-2}	0.085	3.16×10^{-3}
H505A-B	50	MFR	mQ water	9.42	3.15×10^{-3}	1.24×10^{-2}	0.084	3.18×10^{-3}
H506A-E	50	MFR	equil. pH 9.45	9.45	3.62×10^{-3}	1.38×10^{-2}	0.076	3.24×10^{-3}
H75A-C	75	MFR	equil. pH 8.85	8.83	2.14×10^{-3}	2.70×10^{-2}	0.071	1.88×10^{-3}

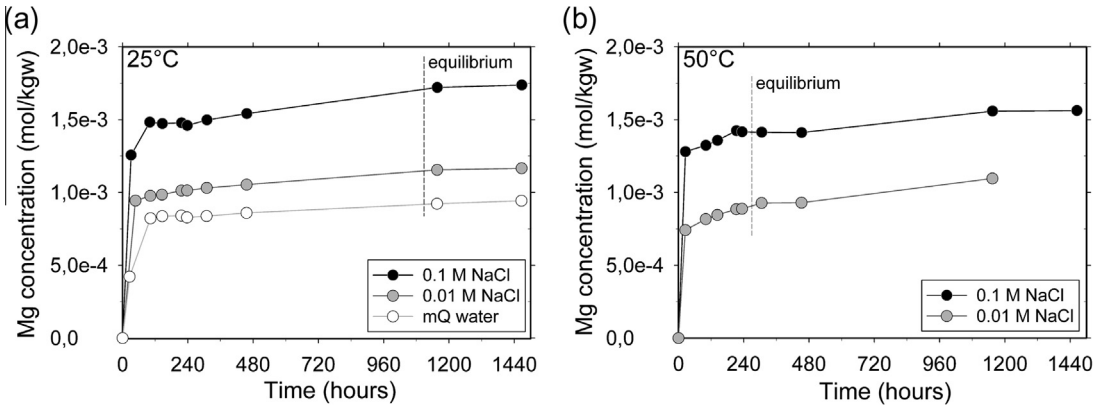


Fig. 4. Evolution of Mg concentration during the course of hydromagnesite solubility experiments at 25 °C (a) and 50 °C (b).

Table 4
Chemical composition of samples retained for calculation of hydromagnesite solubility product at 25 and 50 °C.

Run #	Time (hours)	T (°C)	NaCl (M)	pH (25 °C)	$[Mg^{2+}]$ (mol/kgw)	Alk. (eq/kgw)
Hs25-1i	1157:00	25	0.10	10.40	1.721×10^{-3}	0.00340
-1j	1467:30	25	0.10	10.32	1.738×10^{-3}	0.00355
Hs25-2h	1156:25	25	0.01	10.42	1.155×10^{-3}	0.00279
-2i	1467:00	25	0.01	10.24	1.166×10^{-3}	0.00380
Hs25-3h	1156:00	25	0	10.60	9.223×10^{-4}	0.00190
-3i	1466:30	25	0	10.51	9.431×10^{-4}	0.00204
Hs50-1f	306:00	50	0.10	9.89	1.424×10^{-3}	0.00307
-1g	452:50	50	0.10	9.90	1.413×10^{-3}	0.00289
-1h	1154:30	50	0.10	9.90	1.559×10^{-3}	0.00323
-1i	1465:00	50	0.10	9.93	1.562×10^{-3}	0.00318
Hs50-2f	305:35	50	0.01	9.97	9.256×10^{-4}	0.00196
-2g	452:25	50	0.01	9.97	9.404×10^{-4}	0.00195
-2h	1154:00	50	0.01	9.98	1.096×10^{-3}	0.00233

representative of equilibrium between the solution and hydromagnesite. At 50 °C, a first plateau at constant pH is reached after 300 h of reaction. Higher Mg concentrations are however reached after 1150 h. All three or four last samples were considered for the calculation of the solubility product at 50 °C (see Table 4).

Solution speciation was calculated with PHREEQC based on solution chemistry at equilibrium (Table 4). Calculated ionic strengths and species molalities are reported in Table 5 together with species activity coefficients calculated from the Davies equation, and used to calculate the apparent equilibrium constant $Q_{sp-Hmgs}$ for reaction (1) at the temperature and ionic strength of interest. The corresponding values of hydromagnesite solubility product $K_{sp-Hmgs}$ are then calculated from Eq. (4) and reported in Table 5.

The mean values of log $K_{sp-Hmgs}$ have been plotted as a function of reciprocal temperature, together with literature data, in Fig. 5. Based on the measured solubility product, the standard molar Gibbs free energy of formation of hydromagnesite was calculated using the standard state properties of aqueous species involved in Eq. (1). These values together with data from the literature are listed in Table 6.

Fig. 5 and Table 6 illustrate the large variability of reported hydromagnesite solubility products, which range over ten orders of magnitude. These large discrepancies may in part be due to differences in the crystallinity of the mineral. At the exception of the data reported by Cheng and Li (2010a,b), the solubility product of the natural hydromagnesite used in the present study is higher than those previously reported. Its standard state Gibbs free energy of formation is relatively close to the value reported by

Table 5
Results of solubility product calculations at 25 and 50 °C, and extrapolation to 75 °C. Values of water activity were calculated from Busey and Mesmer (1976).

Run #	T (°C)	pH	I (mol/kgw)	$m(Mg^{2+})$ (mol/kgw)	$\gamma(Mg^{2+})$	$m(CO_3^{2-})$ (mol/kgw)	$\gamma(CO_3^{2-})$	$m(OH^-)$ (mol/kgw)	$\gamma(OH^-)$	$\log Q_{sp}$	a (H_2O)	$\log K_{sp-Hmgs}$
Hs25-1i	25	10.40	0.1042	1.45×10^{-3}	0.369	9.90×10^{-4}	0.369	3.10×10^{-4}	0.779	−33.23	0.996512	−37.36
-1j	25	10.32	0.1043	1.46×10^{-3}	0.368	1.03×10^{-3}	0.368	2.57×10^{-4}	0.779	−33.31	0.996509	−37.44
Hs25-2h	25	10.42	0.0136	8.60×10^{-4}	0.625	7.45×10^{-4}	0.625	2.85×10^{-4}	0.889	−34.93	0.999530	−36.87
-2i	25	10.24	0.0142	8.16×10^{-4}	0.619	1.01×10^{-3}	0.619	1.89×10^{-4}	0.887	−34.88	0.999510	−36.86
Hs25-3h	25	10.60	0.0026	6.81×10^{-4}	0.801	4.31×10^{-4}	0.801	4.05×10^{-4}	0.946	−36.08	0.999910	−37.00
-3i	25	10.51	0.0027	6.87×10^{-4}	0.797	4.83×10^{-4}	0.797	3.30×10^{-4}	0.945	−36.04	0.999906	−36.98
											mean 25 °C = −37.08 ± 0.50 (2σ)	
Hs50-1f	50	9.53	0.1032	1.22×10^{-3}	0.352	6.00×10^{-4}	0.352	2.28×10^{-4}	0.770	−34.74	0.996553	−39.05
-1g	50	9.53	0.1030	1.22×10^{-3}	0.352	5.62×10^{-4}	0.352	2.29×10^{-4}	0.770	−34.85	0.996557	−39.16
-1h	50	9.54	0.1035	1.33×10^{-3}	0.352	6.34×10^{-4}	0.352	2.34×10^{-4}	0.770	−34.43	0.996543	−38.75
-1i	50	9.56	0.1034	1.33×10^{-3}	0.352	6.34×10^{-4}	0.352	2.45×10^{-4}	0.770	−34.39	0.996544	−38.71
Hs50-2f	50	9.54	0.0126	7.64×10^{-4}	0.620	2.90×10^{-4}	0.620	2.03×10^{-4}	0.887	−37.12	0.999562	−39.09
-2g	50	9.54	0.0127	7.78×10^{-4}	0.619	2.88×10^{-4}	0.619	2.02×10^{-4}	0.887	−37.10	0.999561	−39.08
-2h	50	9.57	0.0131	8.79×10^{-4}	0.615	3.54×10^{-4}	0.615	2.15×10^{-4}	0.886	−36.42	0.999547	−38.43
											mean 50 °C = −38.90 ± 0.54 (2σ)	
											extrapolation to 75 °C = −40.95	

Robie and Hemingway (1995), but distinctly higher than that of Xiong (2011). The solubility reported by Cheng and Li (2010a,b) is much higher, but should be considered with much caution since the authors did not apparently monitor pH nor dissolved CO_2 concentration in their experiments, and assume equilibrium was attained after six hours only of equilibration time. The differences observed with the data reported by Xiong (2011) may also be due to the lack of control of the actual CO_2 pressure and temperature in the latter experiments.

The mean reaction enthalpy between 25 and 50 °C (-287.8 ± 81 kJ mol^{-1}) is within experimental uncertainty from the value that can be calculated from the data generated by SUPCRT92. The SUPCRT92 reaction enthalpy and reaction heat capacity at 50 °C were therefore used to extrapolate our data to 75 °C, assuming constant heat capacity between 50 and 75 °C. The corresponding data point has been reported in Table 5, and plotted in Fig. 5. Retrieved solubility products were entered into PHREEQC llnl.dat database in order to accurately calculate solution saturation state with respect to hydromagnesite in our growth experiments.

4.2. Hydromagnesite growth kinetics

4.2.1. Control of the precipitating phase

Speciation calculation with PHREEQC indicates that our experimental solutions are not only supersaturated with respect to hydromagnesite, but also with respect to magnesite (Ω_{Mgs} up to 130 in experiments at 25 °C) and artinite $Mg_2CO_3(OH)_2{\cdot}3H_2O$. Although formation of magnesite is unlikely at temperatures of 75 °C and lower (Hänchen et al., 2008; Saldi et al., 2009), and artinite is expected to form only at temperatures lower than ca. 15 °C (Königsberger et al., 1999), a variety of hydrated Mg-carbonate minerals may form, whose thermodynamic parameters are poorly known (e.g. Davies and Bubela, 1973; Hopkinson et al., 2012). In addition, a few experimental solutions were slightly supersaturated with respect to brucite at 25 °C and 50 °C ($\Omega_{brucite}$ up to 3). It was thus important to control the nature of the precipitating mineral phase.

To this extent, X-ray diffraction and SEM observations were systematically performed on all solids recovered at the end of the experiments. Analyses did not reveal the presence of any other mineral phase than hydromagnesite. The mineral overgrowths occur under the form of agglomerated or individualized single crystals with a "platelet" shape similar to that of the seeds (Fig. 6a–c). Thermo-gravimetric analyses, performed on a few samples, show patterns similar to the seeds' (Appendix A, red curve).

4.2.2. Evolution of the reactive surface area

Determining the evolution of reactive surface area during the course of growth experiments is critical to correctly normalize growth rates. BET measurements performed on the finally recovered minerals indicate that their specific surface area does not vary, within uncertainties, during the course of the experiments. However, upon mineral growth, the mass of seeds increases, thus providing more

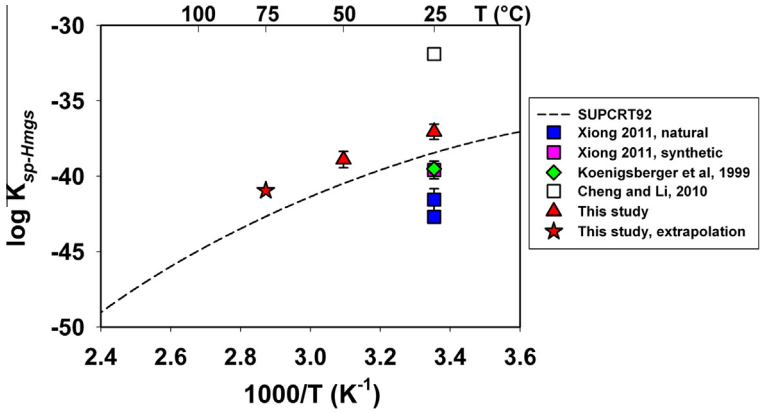


Fig. 5. Logarithm of the solubility product of hydromagnesite obtained in this study versus reciprocal temperature, and comparison to literature values.

Table 6
Values of hydromagnesite solubility product at 25 °C and standard state properties of hydromagnesite (25 °C, 1 bar) reported in the literature and obtained in this study. Bold values in the upper table are the values obtained or used in this study. The standard state properties of aqueous and gaseous species used for determination of the standard Gibbs free energy of formation of hydromagnesite in the present study are reported in the lower table.

Hydromagnesite type	log K_{sp} (25 °C)	ΔG_f^0 kJ/mol	S_f^0 J/mol/K	ΔH_f^0 kJ/mol	Cp^0 J/mol/K	Reference
	−38.45	−5864.66	541.3	**−6514.9**	**571.1**	SUPCRT92, taken from Helgeson (1978)
Natural		−5864.2	503.7	−6514.9		Robie and Hemingway (1995)
Synthetic		−5871.5				Königsberger et al. (1992)
Synthetic	−39.51	−5870.2	520.0	−6516.0		Königsberger et al. (1999)
Natural	−31.9	−5827				Cheng and Li (2010a,b)
Natural	−41.56	−5889 ± 4				Xiong (2011)
Natural	−42.70	−5896 ± 2				Xiong (2011)
Synthetic	−39.59	−5878 ± 3				Xiong (2011)
Natural	**−37.08**	**−5855.6 ± 3**				**This study**
Aqueous species		ΔGf^0 kJ/mol	Sf^0 J/mol/K	ΔHf^0 kJ/mol	Cp^0 J/mol/K	
Mg^{2+}		−454.0	−138.1	−466.0	−22.3	Shock and Helgeson (1988)
CO_3^{2-}		−527.98	−50.00	−675.24	−289.53	Shock and Helgeson (1988)
$CO_{2(g)}$		−394.36	213.74	−393.51	37.24	SUPCRT92
HCO_3^-		−586.77	91.2	−691.99	−35.40	Wagman et al. (1982)
H_2O		−237.13	69.95	−285.83	75.19	Wagman et al. (1982)
OH^-		−157.24	−10.75	−229.99	−148.5	Wagman et al. (1982)

total surface on which further growth may proceed. In experiment H506 (Table 3) for instance, the precipitated mineral mass equals that of the initial seeds, although in most experiments, the gain is between 7% and 50% of the initial seeds mass.

Observations of hydromagnesite pristine crystals morphology reveal that most of their surface is constituted by the (1 0 0) face (plane surfaces of platelets shown in Fig. 1a). This morphology suggests that most of the growth proceeds at the crystal edges. Therefore, crystal growth creates surface mostly through enlargement of the (1 0 0) face, while the reactive surface area constituted by the edges remains to a large extent unchanged. Based on pictures of selected pristine crystals, we estimate that edges represent roughly 5–10% of the total platelet surface in the initial material.

Grinding creates many edges growth sites through the breaking of crystals (see Fig 6b, which shows the fractured aspect of crystal edges). Small crystal fragments have a larger proportion of their total surface constituted by edges, such that the measured BET surface area of the seeds can be assumed to be a relatively good estimate of the actual reactive surface area. At the end of growth experiments, recovered minerals are on average larger in size (and surface) than the initial highly fragmented seed material, while their thickness does not significantly vary. Some crystals exhibit an automorphic shape with a fully developed (1 0 0) face (Fig. 6c), which presumably developed from

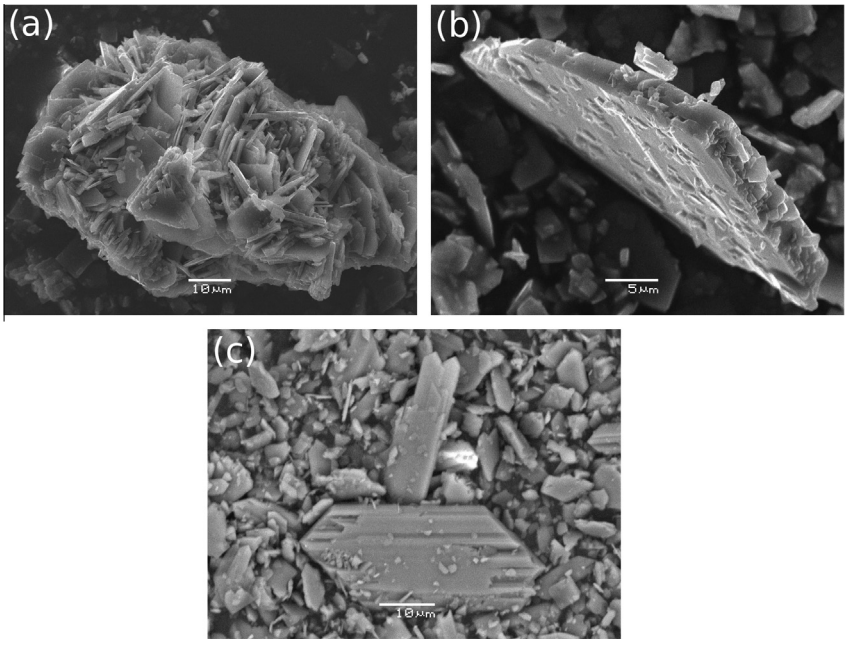


Fig. 6. SEM images of seed crystals after growth experiments. (a) Hydromagnesite agglomerate formed during precipitation at 25 °C (secondary electrons). (b) Close-up view of the edge of one hydromagnesite crystal grown at 25 °C (SE image). (c) BSE image of individual hydromagnesite crystals obtained after growth at 75 °C. The (1 0 0) face is clearly visible.

crystal fragments. These observations confirm that growth proceeds mainly from crystal edges.

Because estimating the surface represented by edges in the grinded seed material is a particularly difficult task, we used the specific BET surface area of this material as a proxy for the "reactive" surface area, which was used to normalize all growth rates. It is however likely that this assumption overestimates the actual reactive surface area, since possibly unreactive (1 0 0) faces represent a significant proportion of the initially measured surface. The important point here, however, is that we assumed that the surface of edges varied negligibly during the course of growth experiments.

4.2.3. Hydromagnesite growth rates as a function of saturation state

Fig. 7 provides two examples of the evolution of Mg concentration and the approach of steady-state during the course of experiments performed respectively at 25 °C using the low temperature mixed-flow reactor setting and at 50 °C in the classical mixed-flow reactor system. The results of all steady-state hydromagnesite experiments are summarized in Tables 7 and 8. The results of daily rate calculations from experiments at 25 °C are reported in Appendix B.

The logarithm of Eq. (8) is written:

$$\log R = \log(k_{Hmgs}) + n \log(\Omega_{Hmgs}^{0.2} - 1) \quad (12)$$

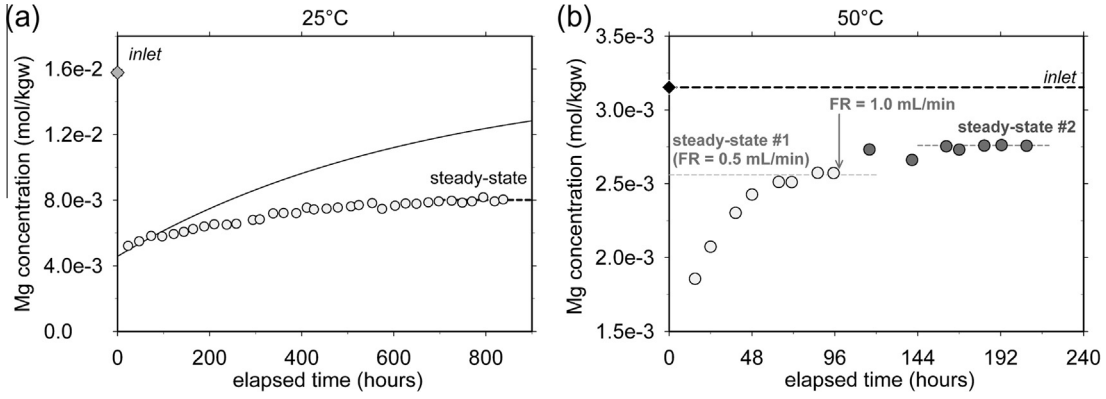


Fig. 7. Representative evolution of Mg concentration in the outlet fluid as a function of time during experiments performed at 25 °C (exp. H10, a), and at 50 °C (exp. H505, b). On (a), the solid line represents the theoretical evolution of Mg concentration if no precipitation was taking place. On (b), the graph presents a series of two experiments with different flow rates performed on the same mineral seeds. Analytical uncertainty is smaller than the symbol size.

Table 7
Results of steady-state precipitation experiments performed at 25 and 30 °C.

Exp. #	T (°C)	Ω_{Hmgs}	Outlet pH 25 °C	Exp. pH @ T	I	$[Mg]_{inlet} \times 10^2$ (mol/kgw)	$\Delta[Mg] \times 10^3$ (mol/kgw)	Alk. $\times 10^2$ (eq/L)	$a_{Mg^{2+}} \times 10^3$	$a_{CO_3^{2+}} \times 10^3$	$\frac{a_{Mg}^{2+}}{a_{CO_3^{2-}}}$	Seed mass (g)	FR (mL/h)	Rate $\times 10^{15}$ (mol/cm^2/s)
H9	*Did not reach steady state*													
H10	25	151.2 ± 33.8	9.66(2)	9.66	0.090	1.578	7.641 ± 0.296	0.879(5)	2.497	0.504	4.95	1.5155	0.766	6.03 ± 0.69
H11	25	165.2 ± 27.7	9.44(2)	9.44	0.088	2.149	10.663 ± 0.357	1.088(2)	3.345	0.464	7.21	1.5214	0.693	7.63 ± 0.83
H12	25	446.0 ± 101.4	9.49(2)	9.49	0.098	2.559	14.419 ± 0.359	1.255(10)	3.330	0.560	5.95	1.5054	0.742	11.09 ± 1.11
H6	30	112.6 ± 15.8	9.20(1)	9.11	0.120	1.712	4.829 ± 0.137	1.406(9)	3.574	0.389	9.18	0.8081	1.057	9.85 ± 1.03
H8	30	263.4 ± 32.8	9.20(1)	9.11	0.122	2.697	12.821 ± 0.256	1.535(6)	4.063	0.411	9.88	0.8016	1.003	25.04 ± 2.39

Table 8
Results of steady-state precipitation experiments performed at 50 and 75 °C with titanium mixed-flow reactors.

Exp. #	T (°C)	Ω_{Hmgs}	outlet pH 25 °C	exp. pH at T	I	$[Mg]_{inlet}$ x 10^2 (mol/kgw)	Δ [Mg] x 10^3 (mol/kgw)	Alk. x 10^2 (eq/L)	$a_{Mg^{2+}} \times 10^3$	$a_{CO_3^{2+}} \times 10^3$	$\frac{a_{Mg}^{2+}}{a_{CO_3^{2-}}}$	Seed mass (g)	FR (mL/h)	Rate $\times 10^{15}$ (mol/cm^2/s)
H504B	50	1.9 ± 0.3	9.13(2)	8.85	0.102	2.591×10^{-3}	0.154 ± 0.030	1.132(1)	0.694	0.314	2.21	1.0314	0.248	3.47 ± 0.85
H504C	50	4.7 ± 1.8	9.35(2)	9.01	0.102	2.616×10^{-3}	0.533 ± 0.049	1.172(8)	0.577	0.417	1.39	1.1168	0.396	17.72 ± 2.56
H504D	50	16.0 ± 4.9	9.33(3)	9.08	0.103	2.616×10^{-3}	0.318 ± 0.027	1.222(4)	0.620	0.482	1.29	1.1168	0.689	18.34 ± 2.51
H505A	50	41.7 ± 2.7	9.34(1)	9.09	0.105	3.150×10^{-3}	0.603 ± 0.020	1.385(8)	0.667	0.556	1.20	1.0317	0.499	27.27 ± 2.31
H505B	50	90.4 ± 26.3	9.38(3)	9.13	0.105	3.150×10^{-3}	0.369 ± 0.035	1.426(2)	0.704	0.600	1.17	1.0317	0.988	33.07 ± 5.35
H506A	50	27.1 ± 7.9	9.32(1)	8.98	0.099	3.620×10^{-3}	0.893 ± 0.026	1.510(1)	0.727	0.506	1.44	0.9071	0.394	36.29 ± 3.44
H506B	50	57.4 ± 7.4	9.28(1)	9.03	0.099	3.620×10^{-3}	0.707 ± 0.041	1.539(2)	0.753	0.557	1.35	0.9071	0.697	50.84 ± 5.64
H506C	50	104.1 ± 11.8	9.32(1)	9.07	0.099	3.620×10^{-3}	0.615 ± 0.032	1.557(5)	0.773	0.598	1.29	0.9071	1.095	69.52 ± 7.34
H506D	50	166.4 ± 28.6	9.34(1)	9.08	0.100	3.660×10^{-3}	0.471 ± 0.058	1.577(5)	0.819	0.615	1.33	0.9071	1.489	72.46 ± 12.84
H506E	50	184.1 ± 22.1	9.34(1)	9.09	0.100	3.660×10^{-3}	0.392 ± 0.057	1.598(1)	0.819	0.628	1.30	0.9071	1.996	80.67 ± 15.92
H75A	75	7.1 ± 0.4	8.67(0)	8.35	0.102	2.138×10^{-3}	0.638 ± 0.031	2.695(13)	0.334	0.310	1.08	0.9175	0.498	32.40 ± 3.28
H75B	75	28.8 ± 3.8	8.75(1)	8.42	0.102	2.138×10^{-3}	0.549 ± 0.031	2.732(9)	0.370	0.359	1.03	0.9175	1.001	56.06 ± 6.01
H75C	75	44.0 ± 6.0	8.76(1)	8.43	0.102	2.138×10^{-3}	0.444 ± 0.019	2.736(1)	0.390	0.368	1.06	0.9175	1.494	67.70 ± 6.38

Accordingly, the logarithm of hydromagnesite growth rates at 25, 30 and 50 and 75 °C have been plotted as a function of $\log(\Omega_{Hmgs}{}^{0.2} - 1)$ in Figs. 8a–c. The dashed lines correspond to $n = 1$ and such a rate order satisfyingly fits all the data. This indicates that hydromagnesite growth is either diffusion-controlled, or controlled by the direct adsorption of growth units onto mineral surface sites (Nielsen, 1984; Lasaga, 1998). A diffusion control of hydromagnesite growth in our well-mixed experiments is very unlikely because of hydromagnesite very slow growth rates. Indeed, if hydromagnesite growth was diffusion-controlled, the growth rates measured in this study would imply values for the aqueous diffusion coefficients of dissolved magnesium and carbonate species near 10 orders of magnitude lower than the actual values.

The rate constants k_{Hmgs} retrieved with a unit rate order are reported in Table 9, together with the best fit parameters for each temperature series. An Arrhenius plot of rates constants obtained with $n = 1$ is shown in Fig. 8d, which is consistent with an activation energy of 45.5 ± 9 kJ mol^{-1}. Note that this activation energy is much higher than typical activation energies for diffusion-controlled processes (10–18 kJ mol^{-1}, Nielsen, 1984). This further confirms that the linear growth rate likely stems from an adsorption-controlled growth mechanism, with subsequent incorporation of reactants to growth sites (steps, kinks) presumably existing on hydromagnesite crystals edges.

Table 9
Values of rate order n and rate constants k_{Hmgs} obtained from the fit of growth rates plotted in Fig. 9. Best fit values and values obtained with $n = 1$ are reported.

T (°C)	n	log k_{Hmgs} (mol cm^2 s^{-1})	R^2
25	0.85 ± 0.06	-14.37 ± 0.23	0.780
	1	-14.39 ± 0.26	0.756
30	1	-14.06 ± 0.15	–
50	1.08 ± 0.10	-13.46 ± 0.07	0.916
	1	-13.47 ± 0.07	0.911
75	0.84 ± 0.06	-13.22 ± 0.05	0.996
	1	-13.21 ± 0.08	0.959

5. DISCUSSION

5.1. Comparison of growth rates with the literature

Our results indicate that hydromagnesite growth rate obeys a linear rate law consistent with the transition state theory and the simple attachment of growth units at steps and kinks (Lasaga, 1998; Schott et al., 2012). To the best of our knowledge, the only other existing study of hydromagnesite precipitation rates was recently published by Wang and Li (2012). The authors studied hydromagnesite nucleation and growth rate at 80 °C from highly supersaturated ($\Omega_{Hmgs} = 10^9$–10^{15}), high ionic strength solutions, using a "mixed-suspension mixed-product removal

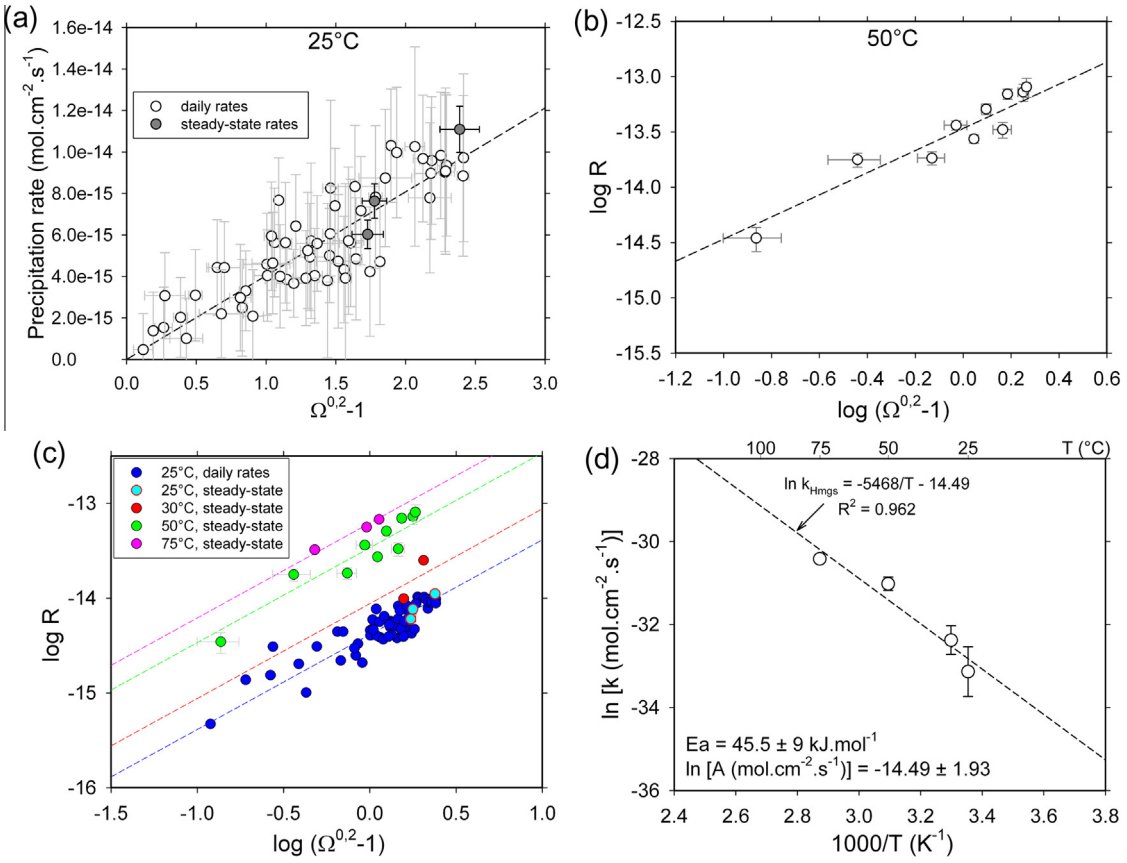


Fig. 8. (a)–(c) Plots of measured hydromagnesite growth rates versus supersaturation. Dashed lines slopes correspond to unit rate order. Error bars on daily growth rates at 25 °C have been omitted for clarity sake. Unless represented, error bars on steady-state rates are smaller than the symbol size. (d) Arrhenius plot of the rate constants obtained for $n = 1$.

crystallizer". According to Wang and Li (2012), their growth rates are consistent with the following rate law:

$$G_L[\mathrm{m/s}] = 3.42 \times 10^{-10}(\Omega^{1/15} - 1)^{0.94} \quad (13)$$

where $\Omega^{1/15}$ stems from an empirical definition of the saturation state by Nielsen (1984). In order to obtain growth rates directly comparable to our data, it is necessary to divide growth rates reported by Wang and Li (2012) by hydromagnesite molar volume ($V_M = 201.57\ \mathrm{cm^3/mol}$). One obtains:

$$R_L[\mathrm{mol/cm^2/s}] = 1.70 \times 10^{-10}(\Omega^{1/15} - 1)^{0.94} \quad (14)$$

When using a rate law of the type of Eq. (14) to fit our data at 75 °C, we obtain a growth rate constant of 2.29×10^{-13} mol/cm^2/s (rate order 0.995). Thus for the same saturation state, our growth rate is nearly three orders of magnitude lower than that of Wang and Li (2012) at 80 °C. Several factors may explain this important discrepancy:

- Different surface area normalization of growth rates were used by Wang and Li (2012) and in this study. The former implicitly considers the reactive surface area to be the geometrical surface of the pseudo-spherical hydromagnesite agglomerates precipitated in their experiments. However, such particles are built by "a large number of thin sheets", which indicates that the actual reactive surface probably exceeds by far the geometrical surface area. On the other hand, in the present study, growth rates were normalized to BET surface area, which likely overestimates the reactive surface area as growth proceeds from the crystal edges (see above). These different normalizations may account in part for the different rates reported in the two studies.
- Nucleation and growth proceeded at extremely high saturation state in Wang and Li (2012) experiments. Rate law (14) indicates a unit rate order, which could reflect a diffusion-limited growth process (Nielsen, 1984). At the mineral surface, it is possible that growth proceeds through spiral growth or two-dimensional nucleation, at a much higher rate than adsorption-controlled growth (Shiraki and Brantley, 1995; Teng et al., 2000).
- High ionic strengths (several mol/kg) used in Wang and Li (2012) experiments decrease water activity, which in turn may facilitate cation dehydration and increase crystal growth rate (e.g. Kowacz and Putnis, 2008).
- It cannot be excluded that the mineral originally precipitated by Wang and Li (2012) is actually not pure hydromagnesite, but contains nesquehonite or dypingite. The authors report the presence of nesquehonite in powders precipitated at 25 or 35 °C, and dypingite at 70 °C. Powders were air-dried at 80 °C for 10 h before SEM observations and XRD analysis, which could have altered their mineralogy. Nesquehonite is indeed known to transform into hydromagnesite within a few tens of hours above 50 °C (Davies and Bubela, 1973) with dypingite being a likely intermediate in this transformation (Hopkinson et al., 2008). It is therefore possible that the nucleation and growth of an additional, more hydrated, Mg-carbonate phase has increased the apparent hydromagnesite growth rates reported by the authors.

5.2. Influence of Mg^{2+} dehydration on Mg-carbonates growth activation energy and growth rates

Metal cations in aqueous solutions are surrounded by a hydration sphere (Burgess, 1999) which they have to lose (or partly lose) prior to incorporation in the crystal edifice. It is widely accepted that this cation dehydration is the rate-controlling step for most ionic crystals precipitation (Nielsen, 1984; Piana et al., 2006; Kowacz et al., 2007). Given the highly hydrated character of Mg^{2+}, numerous authors hypothesized that the reluctance to precipitate the anhydrous form of Mg-carbonates originates in the difficulty to dehydrate Mg^{2+} (e.g. Lippmann, 1973; Sayles and Fyfe, 1973; Pokrovsky and Schott, 2002; Hänchen et al., 2008; Romanek et al., 2009; Saldi et al., 2009; Schott et al., 2009).

Based on this idea, Lippmann (1973) proposed a correspondence between the activation energy for carbonate mineral precipitation, and the hydration enthalpy of the constituting cation. As such, the author estimated the activation energy of magnesite precipitation to be significantly higher than that of calcite. This idea was verified by Arvidson and Mackenzie (2000) who observed that the activation energy of several Ca–Mg-carbonate minerals scales with the amount of Mg in the crystal structure.

Following Lippmann (1973), we may hypothesize that minerals with similar chemistry but different water contents should exhibit different activation energies. Because hydromagnesite contains 0.8 water molecules per magnesium

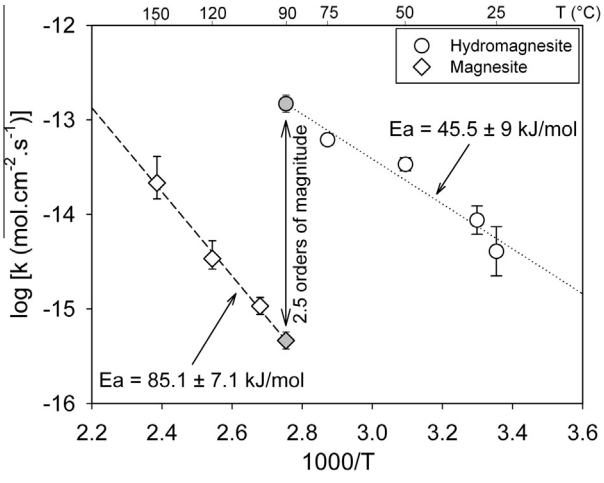


Fig. 9. Comparison of Arrhenius plots for growth rate constants of hydromagnesite in the temperature range 25 °C < T < 75 °C and magnesite in the temperature range 100 °C < T < 200 °C. White data points correspond to experimentally retrieved rate constants, grey-filled points are extrapolations to 90 °C. Magnesite growth rate constants have been taken from Gautier (2012). Hydromagnesite activation energy is significantly lower than magnesite activation energy (see text).

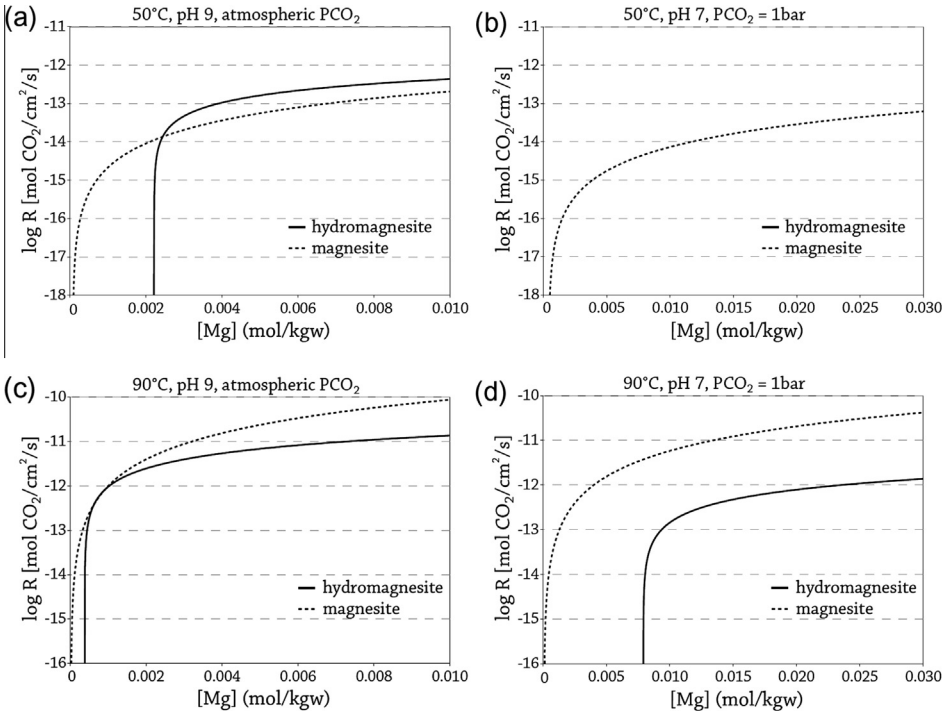


Fig. 10. Hydromagnesite and magnesite growth rates as a function of Mg concentration for different case studies (see text). The absence of hydromagnesite curve in graph (b) reveals that hydromagnesite always remains undersaturated in this simulation. Note that these figures only compare growth rates, and do not provide any information on the minerals' respective nucleation rates in the same conditions.

atom, the lower need for Mg dehydration should result in lower activation energy. The apparent activation energy measured in this study in the temperature range 25–75 °C for hydromagnesite growth rate constant is equal to 45.5 ± 9 kJ mol^{-1} (Fig. 8d), which is lower by approximately 40 kJ mol^{-1} than the activation energy of magnesite growth constant in the temperature range 100 °C < T < 150 °C (see Fig. 9). However, magnesite growth proceeds through spiral growth (Saldi et al., 2009), whereas hydromagnesite is interpreted to grow through the direct incorporation of growth units at the surface steps or kinks. It is thus more rigorous to compare hydromagnesite growth activation energy with the activation energy for magnesite step advancement at the mineral surface, which is as well controlled by the adsorption of growth units onto kinks. Saldi et al. (2009) measured the activation energy for obtuse steps advancement in the temperature range 80 °C < T < 120 °C, and obtained a value of 159 ± 17 kJ mol^{-1}, which is more than 100 kJ mol^{-1} higher than the value measured in this study for hydromagnesite. Thus, our results support the hypothesis that a lesser need for dehydration results in a much lower activation energy of the growth rate constant.

Interestingly, Morales et al. (2012) compared the activation energy of step advancement for anhydrite ($CaSO_4$) between 60 and 120 °C and gypsum ($CaSO_4{\cdot}2H_2O$) between 20 and 80 °C. In contradiction with Lippmann (1973) hypothesis, it was observed that both activation energies are close to 72 kJ mol^{-1}. As stated by Morales et al. (2012), this suggests that anhydrite growth is not limited by Ca^{2+} dehydration. Besides, the large difference between anhydrite and magnesite step advancement activation energy (about 90 kJ mol^{-1}) outlines the large difference between Ca^{2+} and Mg^{2+} hydration state and the rate of exchange of water molecules between their first hydration shell and the bulk of the solution (~4 orders of magnitude, Bleuzen et al., 1997; Larentzos and Criscenti, 2008).

The kinetic rate constants obtained for hydromagnesite and magnesite growth (Gautier, 2012) have been plotted on an Arrhenius diagram in Fig. 9. On the basis of retrieved Arrhenius parameters, the kinetic rate constants were extrapolated to 90 °C. We obtain $\log k_{Hmgs} = -12.83 \pm 0.21$ and $\log k_{Mgs} = -15.33 \pm 0.09$ (mol.cm^{-2}.s^{-1}). Thus at 90 °C, hydromagnesite rate constant is 2.5 orders of magnitude higher than that of magnesite. Note that growth rates normalization to BET surface area likely overestimates hydromagnesite reactive surface area, such that the difference between the two rate constants could be even higher (by up to one order of magnitude). This supports the idea that Mg^{2+} dehydration limits the rate of magnesite precipitation, and that hydrated minerals are less kinetically inhibited than their anhydrous counterparts. Due to the different "bulk" activation energies, this difference is exacerbated at lower temperatures, and tends to be lowered at higher temperatures.

Finally, it should be noted that hydromagnesite precipitation rates remain significantly lower than calcite rates, which are about 6 orders of magnitude higher than magnesite's (Shiraki and Brantley, 1995; Saldi et al., 2009).

5.3. Which consequences for CO_2 mineral sequestration?

Hydromagnesite stores 0.8 mol of CO_2 per mole of Mg precipitated. This ratio is lower than that of magnesite,

but because hydromagnesite forms at ambient temperature, it has attracted interest as a potential sink for CO_2 mineral sequestration (e.g. Teir et al., 2009; Power et al., 2009; Wilson et al., 2009). Furthermore, because the slow magnesite precipitation rate has been suggested to limit the process of forsterite carbonation between 100 and 150 °C (Saldi et al., 2012), it is important to determine whether hydromagnesite precipitation could accelerate the carbonation process (Guyot et al., 2011). Towards this goal we have computed surface area-normalized hydromagnesite and magnesite growth rates as a function of solution composition, at chosen conditions of temperature, pH and pCO_2. Hydromagnesite rates were computed from Eq. (8) with $n = 1$, while magnesite growth rates are given by Saldi et al. (2012):

$$R_{Mgs} = k_{Mgs}(\Omega_{Mgs} - 1)^2 \quad (15)$$

Simulations were performed at pH 9 and atmospheric pCO_2, and pH 7 and $pCO_2 = 1$ bar. The former conditions are representative of surface alteration of ultramafic rocks, including mine tailings (e.g., Bea et al., 2012), while the latter were chosen to assess the influence of a lower pH and higher pCO_2 on hydromagnesite growth kinetics, more typical of mineral carbonation conditions.

In both cases, simulations were performed at 50 and 90 °C while the solution ionic strength was kept close to 0.1 M by adjusting the background NaCl concentration. Magnesite rate constant was extrapolated to 50 °C using the activation energy determined by Gautier, 2012 (see Fig. 9). Note however that this activation energy determined above 100 °C is likely not applicable to such low temperatures (Saldi et al., 2009). The extrapolation to 50 °C should thus be viewed as a maximum estimation of magnesite growth rate. The results of these simulations are presented in Fig. 10.

At pH 9 and 50 °C (Fig. 10a), hydromagnesite growth rates quickly passes magnesite rates after its solubility is reached. The difference in surface area-normalized growth rates remains limited in this simulation (half an order of magnitude), but one should keep in mind that magnesite growth rate is likely overestimated at 50 °C. At pH 9 and 90 °C, magnesite rates always remain higher or equal to hydromagnesite ones. At pH 7, hydromagnesite solubility is never exceeded in the investigated conditions at 50 °C (Fig. 10b), while at 90 °C, hydromagnesite rates always remain far lower than magnesite ones due to its low saturation state.

These simulations reveal that in natural or industrial conditions, hydromagnesite growth rates may exceed magnesite ones only at high pH and relatively low temperatures, while conditions typical for direct forsterite or serpentine carbonation (i.e., slightly acidic pH and high pCO_2) are clearly unfavorable for hydromagnesite growth. Note however that magnesite and hydromagnesite formation are not controlled only by the minerals respective growth rates, but also by their respective nucleation kinetics and possibly by solid-state transformation of hydromagnesite into magnesite. In the present study, we only provide data on growth rates, while nucleation rates and factors controlling mineral transformation remain unknown.

Thus, this could explain why hydromagnesite formation has been observed at temperatures of 120 °C and under 3 bars of CO_2 pressure (Hänchen et al., 2008), and up to 160 °C in batch forsterite carbonation experiments performed in slightly alkaline conditions under low CO_2 pressure (King et al., 2010). In these adverse conditions for hydromagnesite growth, as we have just seen, nucleation kinetics must thus play a crucial role in the apparition of the mineral, which indicates that magnesite nucleation may be even more kinetically inhibited than magnesite growth, as suggested by Lippmann (1973). It is also likely that hydromagnesite, as a hydrated mineral, has a lower surface free energy compared to magnesite, which would facilitate its nucleation. Even so, our results show that hydromagnesite does not provide an easy path for CO_2 sequestration through direct mineral carbonation.

6. CONCLUSION

The present study aimed at investigating the growth kinetics of hydromagnesite $Mg_5(CO_3)_4(OH)_2{\cdot}4H_2O$ and comparing it to that of magnesite, the anhydrous form of Mg-carbonates. Using thermodynamic parameters determined from the solubility of natural hydromagnesite samples, we have studied hydromagnesite growth kinetics as a function of saturation state and temperature from 25 to 75 °C.

Hydromagnesite obeys a linear rate law, which reflects a growth mechanism likely controlled by the adsorption of growth units to active growth sites located on crystal edges. The apparent activation energy of its rate constant is 45.5 ± 9 kJ mol^{-1}, which is more than 100 kJ mol^{-1} lower than activation energy determined for magnesite obtuse step advancement between 80 and 120 °C by Saldi et al. (2009). In addition, hydromagnesite growth rate constant extrapolated to 90 °C exceeds by 2.5 orders of magnitude magnesite growth rate constant at the same temperature.

These results confirm through direct observations the long-standing hypothesis that Mg^{2+} slow dehydration rate is responsible for the sluggish magnesite precipitation kinetics. If part of this inhibition is removed through precipitation of a hydrated Mg-carbonate such as hydromagnesite, growth rates increase significantly compared to the anhydrous form. Moreover, the observed lower activation energy of hydromagnesite confirms the hypothesis by Lippmann (1973) that for a given growth mechanism, carbonate minerals growth activation energy reflects the extent of cation hydration.

This original dataset shall prove to be useful for various fields of research, including the industrial synthesis of hydromagnesite as a fire retardant (Hollingbery and Hull, 2010a), the understanding of the evolution of MgO or $Mg(OH)_2$-based engineered barriers for CO_2 buffering in nuclear waste repositories (Zhang et al., 2000; Xiong and Lord, 2008), the quantification and optimization of CO_2 sequestration through alteration of ultramafic mine tailings and precipitation of hydromagnesite (Wilson et al., 2009), and the understanding of the role of biofilms and stromatolites in precipitating hydrous Mg-carbonates in alkaline, Mg-rich environments (Walter et al., 1973; Braithwaite

and Zedef, 1996; Kazmierczak et al., 2011; Mavromatis et al., 2012; Shirokova et al., 2013). Overall, hydromagnesite growth kinetics at ambient temperature remain slow, and the assumption of its equilibrium precipitation in reactive transport models (e.g. Bea et al., 2012) is overly simplifying.

Simulations of hydromagnesite and magnesite growth rates as a function of solution composition indicate that hydromagnesite could grow faster than magnesite only at temperatures lower than ca. 50–60 °C and alkaline pH, which explains its formation as a result of surface alteration of ultramafic rocks. On the contrary, under typical conditions foreseen for CO_2 mineral sequestration by direct carbonation of Mg–silicates, hydromagnesite growth is not favored.

However, experimental evidences suggest that hydromagnesite is often a precursor of magnesite formation at hydrothermal temperatures (Sayles and Fyfe, 1973; Zhang et al., 2000; Hänchen et al., 2008). In surface sedimentary environments, the occurrence of magnesite in association with a variety of Mg-carbonate phases, including hydromagnesite, nesquehonite and dypingite, has prompted several authors to propose that magnesite could form over a timescale of years through the dessication of hydrated Mg-carbonate phases (Graf et al., 1961; Renault and Stead, 1990; Deelman, 2011).

Therefore, accurate predictions of the formation, growth and evolution of Mg-carbonate phases in natural as well as industrial systems clearly require to better constraining the respective nucleation kinetics of the various Mg-carbonate phases. Furthermore, understanding the mechanisms that trigger mineralogical transformation of hydromagnesite or other hydrated Mg-carbonates into the less reactive magnesite could provide a pathway for long-term low-temperature CO_2 sequestration strategies.

ACKNOWLEDGMENTS

The authors wish to thank Carole Causserand for help with chemical analysis, Michel Thibaut for performing X-ray diffraction measurements, Alain Castillo for technical assistance with high and low-temperature reactors, and Guillaumbe Lambaré (INSA Toulouse) for kindly performing thermo-gravimetric analysis. Our gratitude goes to Patrick Cabrol who provided us with pristine natural hydromagnesite samples from the Réseau André Lachambre cave network. This work was sponsored by the ANR (French National Agency for Research), within the framework of the CO2-FIX project under contract ANR-08-PCO2-003. Finally, we wish to thank François Guyot and an anonymous reviewer for their insightful comments on a previous version of this manuscript, and Chen Zhu for his editorial assistance.

APPENDIX A. THERMOGRAVIMETRIC ANALYSIS OF HYDROMAGNESITE SEEDS

In order to verify that the stoichiometry of our seed material corresponds to the formula $Mg_5(CO_3)_4(OH)_2{\cdot}4H_2O$, we performed thermo-gravimetric analyses (TGA) using a Netzsch STA449-F3 TG/DSC Analyzer. Analyses were conducted under an argon atmosphere, at a heating rate of 10 °C min^{-1} between 30 and 1000 °C, with approximately 800 mg of sample. Hydromagnesite thermal decomposition proceeds through the following reaction (Beck, 1950; Sawada et al., 1978):

$$Mg_5(CO_3)_4(OH)_2 \cdot 4H_2O = 5MgO + 4CO_2 + 5H_2O \quad (16)$$

The four molecules of crystalline water are lost first, above 210 °C, leading to a weight loss of 15.4%. This first step is followed at higher temperature by dehydroxylation, and finally by the loss of four CO_2 molecules. The overall weight loss is theoretically 56.9%, while the exact decomposition mechanism depends on the heating rate and grain size (Hollingbery and Hull, 2010b).

Results of TGA are provided in Fig. A1. The overall weight loss is 56.6%, thus closely matching the expected weight loss of $Mg_5(CO_3)_4(OH)_2{\cdot}4H_2O$. The different decomposition steps match with those reported in the literature, with an initial loss of 15.06% corresponding to 4 H_2O molecules. The rest of the profile exhibits several independent decomposition steps, and closely resembles the hydromagnesite's TGA at a heating rate of 30 °C min^{-1} reported by Hollingbery and Hull (2012). In particular, the rapid weight loss around 500 °C has been interpreted to result from a rapid release of CO_2 from the crystal structure (Khan et al., 2001). Our TG analysis therefore confirms that our natural hydromagnesite contains four molecule of crystalline water.

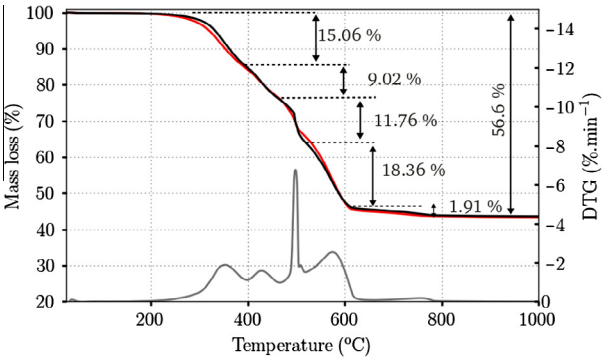


Fig. A1. Results of thermo-gravimetric analysis performed on the initial seed material (black curve) as well as on the precipitated material at 25 °C (exp. H11, red). The grey curve is the differential thermo-gravimetry (DTG), corresponding to the rate of weight loss. Four main decomposition steps are visible, at 353 °C, 428 °C, 498 °C and 575 °C, respectively. The first DTG peak corresponds to loss of four molecules of crystalline water, while the other peaks correspond to non-stoichiometric losses of CO_2 and H_2O. Small variations in the TGA curve between the seed and the precipitated material may be related to the bigger grain size of the precipitated material (Hollingbery and Hull, 2010b). (For interpretation of the references to color in this figure legend, the reader is referred to the web version of this article.)

APPENDIX B.

See Table B1.

Table B1
Results of daily rate calculations from discontinuous mixed-flow reactor experiments performed at 25 °C. Uncertainties on saturation state come from analytical uncertainties on pH, Mg concentration and alkalinity, as well as from the averaging of daily rates over three successive days. Uncertainties on growth rates were calculated based on error propagation from different sources of uncertainty (Mg concentration, flow rate, BET surface area).

Exp. #	Ω_{Hmgs}	±	Rate (mol/cm^2/s)	±	Exp. #	Ω_{Hmgs}	±	Rate (mol/cm^2/s)	±
H9	1.8	0.6	4.70×10^{-16}	1.74×10^{-15}	H11	5.9	2.9	1.01×10^{-15}	1.94×10^{-15}
	3.2	0.9	1.54×10^{-15}	1.94×10^{-15}		14.2	5.4	4.43×10^{-15}	2.21×10^{-15}
	5.1	1.0	2.03×10^{-15}	1.92×10^{-15}		25.1	5.4	2.08×10^{-15}	2.24×10^{-15}
	7.4	1.3	3.09×10^{-15}	2.20×10^{-15}		35.2	4.7	5.94×10^{-15}	2.62×10^{-15}
	20.5	2.0	2.49×10^{-15}	2.33×10^{-15}		44.8	4.9	5.63×10^{-15}	2.91×10^{-15}
	21.9	2.9	3.30×10^{-15}	1.92×10^{-15}		53.1	3.3	6.42×10^{-15}	2.49×10^{-15}
	32.4	15.8	4.59×10^{-15}	2.46×10^{-15}		64.1	7.7	5.25×10^{-15}	2.81×10^{-15}
	45.8	19.1	3.85×10^{-15}	1.49×10^{-15}		90.5	10.7	8.26×10^{-15}	4.24×10^{-15}
						90.0	10.2	6.06×10^{-15}	2.33×10^{-15}
						120.1	19.9	5.61×10^{-15}	3.08×10^{-15}
						138.2	1.9	7.17×10^{-15}	2.61×10^{-15}
						100.9	35.4	4.73×10^{-15}	3.22×10^{-15}
						111.8	10.1	3.92×10^{-15}	4.55×10^{-15}
						96.5	5.2	7.40×10^{-15}	2.78×10^{-15}
						116.6	27.1	5.72×10^{-15}	3.55×10^{-15}
						177.1	10.2	4.71×10^{-15}	3.03×10^{-15}
						167.2	15.0	7.82×10^{-15}	3.45×10^{-15}
H10	2.4	0.1	1.38×10^{-15}	1.87×10^{-15}	H12	3.4	2.4	3.07×10^{-15}	2.07×10^{-15}
	12.2	3.0	4.43×10^{-15}	2.31×10^{-15}		13.4	7.6	2.20×10^{-15}	2.12×10^{-15}
	19.7	4.5	2.98×10^{-15}	2.57×10^{-15}		36.0	15.1	4.64×10^{-15}	2.45×10^{-15}
	32.8	8.5	4.04×10^{-15}	2.20×10^{-15}		127.6	47.7	8.34×10^{-15}	2.95×10^{-15}
	40.9	0.4	4.01×10^{-15}	2.49×10^{-15}		203.4	10.4	1.03×10^{-14}	2.73×10^{-15}
	39.9	0.6	7.67×10^{-15}	2.05×10^{-15}		218.2	16.5	9.98×10^{-15}	3.15×10^{-15}
	37.1	2.2	5.64×10^{-15}	2.62×10^{-15}		189.6	71.5	8.75×10^{-15}	3.31×10^{-15}
	51.3	16.4	3.67×10^{-15}	1.64×10^{-15}		271.2	32.8	1.03×10^{-14}	4.81×10^{-15}
	67.5	0.2	5.72×10^{-15}	3.75×10^{-15}		387.0	39.5	9.35×10^{-15}	3.40×10^{-15}
	74.1	26.8	5.59×10^{-15}	2.31×10^{-15}		322.1	85.7	7.79×10^{-15}	3.62×10^{-15}
	66.4	19.1	4.94×10^{-15}	2.58×10^{-15}		329.0	47.4	9.59×10^{-15}	3.07×10^{-15}
	89.2	3.7	5.01×10^{-15}	2.27×10^{-15}		363.8	6.5	9.83×10^{-15}	3.05×10^{-15}
	86.5	6.4	3.80×10^{-15}	3.72×10^{-15}		297.8	34.3	9.68×10^{-15}	3.06×10^{-15}
	71.4	8.6	4.04×10^{-15}	2.28×10^{-15}		326.1	65.7	8.97×10^{-15}	3.19×10^{-15}
	62.4	13.8	3.92×10^{-15}	2.29×10^{-15}		380.7	41.5	9.03×10^{-15}	3.83×10^{-15}
	109.6	8.7	4.33×10^{-15}	2.57×10^{-15}		383.2	24.7	9.08×10^{-15}	4.01×10^{-15}
	129.3	11.0	4.85×10^{-15}	2.94×10^{-15}		464.6	8.1	9.72×10^{-15}	4.04×10^{-15}
	155.7	8.2	4.23×10^{-15}	3.12×10^{-15}		462.7	29.2	8.85×10^{-15}	3.87×10^{-15}

REFERENCES

Aagaard P. and Helgeson H. C. (1982) Thermodynamic and kinetic constraints on reaction rates among minerals and aqueous solutions I. Theoretical considerations. *Am. J. Sci.* **282**, 237–285.

Alderman A. R. and Von Der Borch C. C. (1960) Occurrence of Hydromagnesite in Sediments in South Australia. *Nature* **188**, 931.

Arvidson R. S. and Mackenzie F. T. (2000) Temperature dependence of mineral precipitation rates along the $CaCO_3$–$MgCO_3$ join. *Aquat. Geochem.* **6**, 249–256.

Ballirano P., De Vito C., Ferrini V. and Mignardi S. (2010) The thermal behaviour and structural stability of nesquehonite, $MgCO_3{\cdot}3H_2O$, evaluated by in situ laboratory parallel-beam X-ray powder diffraction: New constraints on CO_2 sequestration within minerals. *J. Hazard. Mater.* **178**, 522–528.

Bea S. A., Wilson S. A., Mayer K. U., Dipple G. M., Power I. M. and Gamazo P. (2012) Reactive transport modeling of natural carbon sequestration in ultramafic mine tailings. *Vadose Zone J.* **11**(2).

Beck C. W. (1950) Differential thermal analysis curves of carbonate minerals. *Am. Mineral.* **35**, 985–1013.

Bénézeth P., Saldi G. D., Dandurand J. L. and Schott J. (2011) Experimental determination of the solubility product of magnesite at 50 to 200 °C. *Chem. Geol.* **286**, 21–31.

Bénézeth P., Chen J., Qafoku O., Schaef H. T., Thompson C. J., Pearce C., Felmy A. R., Bonneville A., Rosso K. M. and Loring J. S. (2013) In situ IR spectroscopic study of forsterite carbonation in wet-scCO_2. *Mineral. Mag.* **77**, 685.

Bleuzen A., Pittet P. A., Helm L. and Merbach A. E. (1997) Water exchange on Magnesium(II) in aqueous solution: a variable temperature and pressure ^{17}O NMR study. *Magn. Reson. Chem.* **35**, 765–773.

Blum A. E. and Lasaga A. C. (1987) Monte Carlo simulations of surface reaction rate laws. *Aquat. Surface Chem.*, 255–292.

Braithwaite C. J. R. and Zedef V. (1996) Hydromagnesite stromatolites and sediments in an alkaline lake, Salda Golu, Turkey. *J. Sediment. Res.* **66**, 991–1002.

Burgess J. (1999) *Ions in Solution: Basic Principles of Chemical Interactions*. Woodhead Publishing.

Busey R. H. and Mesmer R. E. (1976) The ionization of water in NaCl media to 300 °C. *J. Solution Chem.* **5**, 147–152.

Cheng W. and Li Z. (2010a) Nucleation kinetics of nesquehonite $MgCO_3{\cdot}3H_2O$ in the $MgCl_2$–Na_2CO_3 system. *J. Cryst. Growth* **312**, 1563–1571.

Cheng W. and Li Z. (2010b) Controlled supersaturation precipitation of hydromagnesite for the $MgCl_2$–Na_2CO_3 system at elevated temperatures: chemical modeling and experiment. *Ind. Eng. Chem. Res.* **49**, 1964–1974.

Cheng W., Li Z. and Demopoulos G. P. (2009) Effects of temperature on the preparation of magnesium carbonate hydrates by reaction of $MgCl_2$ with Na_2CO_3. *Chin. J. Chem. Eng.* **17**, 661–666.

Davies P. J. and Bubela B. (1973) The transformation of nesquehonite into hydromagnesite. *Chem. Geol.* **12**, 289–300.

Deelman J. C. (2011). *Low-temperature formation of magnesite and dolomite*, 2.3 ed. .

Felmy A. R., Qafoku O., Arey B. W., Hu J. Z., Hu M., Schaef H. T., Ilton E. S., Hess N. J., Pearce C. I., Feng J. and Rosso K. M. (2012) Reaction of water-saturated supercritical CO_2 with forsterite: evidence for magnesite formation at low temperatures. *Geochim. Cosmochim. Acta* **91**, 271–282.

Fischbeck R. and Müller G. (1971) Monohydrocalcite, hydromagnesite, nesquehonite, dolomite, aragonite, and calcite in speleothems of the Fränkische Schweiz, Western Germany. *Contr. Mineral. Petrol.* **33**, 87–92.

Frost R. L., Bahfenne S., Graham J. and Martens W. N. (2008) Thermal stability of artinite, dypingite and brugnatellite – Implications for the geosequestration of greenhouse gases. *Thermochim. Acta* **475**, 39–43.

Gautier Q. (2012) Cinétiques de précipitation de minéraux carbonatés magnésiens, influence de ligands organiques, et conséquences pour la séquestration minérale du CO_2. Thèse de l'Université Paris Est, 237pp. http://pastel.archives-ouvertes.fr/pastel-00806512.

Goto A., Arakawa H., Morinaga H. and Sakiyama T. (2003) The occurrence of hydromagnesite in bottom sediments from Lake Siling, central Tibet: implications for the correlation among $\delta^{18}O$, $\delta^{13}C$ and particle density. *J. Asian Earth Sci.* **21**, 979–988.

Graf D. L., Eardley A. J. and Shimp N. F. (1961) A preliminary report on magnesium carbonate formation in Glacial Lake Bonneville. *J. Geol.* **69**, 219–223.

Guyot F., Daval D., Dupraz S., Martinez I., Ménez B. and Sissmann O. (2011) CO_2 geological storage: The environmental mineralogy perspective. *C. R. Geosci.* **343**, 246–259.

Helgeson H. C. (1978) Summary and critique of the thermodynamic properties of rock-forming minerals. *Am. J. Sci.* **278 A**(1), 229.

Hänchen M., Prigiobbe V., Baciocchi R. and Mazzotti M. (2008) Precipitation in the Mg-carbonate system: effects of temperature and CO_2 pressure. *Chem. Eng. Sci.* **63**, 1012–1028.

Hollingbery L. A. and Hull T. R. (2010a) The fire retardant behaviour of huntite and hydromagnesite – A review. *Polym. Degrad. Stab.* **95**, 2213–2225.

Hollingbery L. A. and Hull T. R. (2010b) The thermal decomposition of huntite and hydromagnesite: A review. *Thermochim. Acta* **509**, 1–11.

Hollingbery L. A. and Hull T. R. (2012) The thermal decomposition of natural mixtures of huntite and hydromagnesite. *Thermochim. Acta* **528**, 45–52.

Hopkinson L., Rutt K. and Cressey G. (2008) The transformation of nesquehonite to hydromagnesite in the system CaO–MgO–H_2O–CO_2: An experimental spectroscopic study. *J. Geol.* **116**, 387–400.

Hopkinson L., Kristova P., Rutt K. and Cressey G. (2012) Phase transitions in the system MgO–CO_2–H_2O during CO_2 degassing of Mg-bearing solutions. *Geochim. Cosmochim. Acta* **76**, 1–13.

Kazmierczak J., Kempe S., Kremer B., López-García P., Moreira D. and Tavera R. (2011) Hydrochemistry and microbialites of the alkaline crater lake Alchichica, Mexico. *Facies* **57**, 543–570.

Khan N., Dollimore D., Alexander K. and Wilburn F. W. (2001) The origin of the exothermic peak in the thermal decomposition of basic magnesium carbonate. *Thermochim. Acta* **367–368**, 321–333.

King H. E., Plümper O. and Putnis A. (2010) Effect of secondary phase formation on the carbonation of olivine. *Environ. Sci. Technol.* **44**, 6503–6509.

Königsberger E., Königsberger L. C. and Gamsjäger H. (1999) Low-temperature thermodynamic model for the system Na_2CO_3–$MgCO_3$–$CaCO_3$–H_2O. *Geochim. Cosmochim. Acta* **63**, 3105–3119.

Kowacz M. and Putnis A. (2008) The effect of specific background electrolytes on water structure and solute hydration: Consequences for crystal dissolution and growth. *Geochim. Cosmochim. Acta* **72**, 4476–4487.

Kowacz M., Putnis C. and Putnis A. (2007) The effect of cation/anion ratio in solution on the mechanism of barite growth at constant supersaturation: role of the desolvation process on the growth kinetics. *Geochim. Cosmochim. Acta* **71**, 5168–5179.

Lasaga A. C. (1995) Fundamental approaches in describing mineral and dissolution rates. *Rev. Mineral.* **31**, 23–86.

Lasaga A. C. (1998) *Kinetic theory in the earth sciences*. Princeton University Press, 811pp.

Lindsay W. T. (1989). *Chemistry of steam cycle solutions: principles*. In The ASME Handbook on Water Technology for Thermal Power Systems (ed. P. Cohen).

Langmuir D. (1965) Stability of carbonates in the system MgO–CO_2–H_2O. *J. Geol.* **73**, 730–754.

Larentzos J. P. and Criscenti L. J. (2008) A molecular dynamics study of alkaline earth metal-chloride complexation in aqueous solution. *J. Phys. Chem. B* **112**, 14243–14250.

Lippmann F. (1973) *Sedimentary carbonate minerals*. Springer-Verlag, Berlin, 228pp.

Loring J. S., Thompson C. J., Zhang C., Wang Z., Schaef H. T. and Rosso K. M. (2012) In situ infrared spectroscopic study of brucite carbonation in dry to water-saturated supercritical carbon dioxide. *J. Phys. Chem. A* **116**, 4768–4777.

Marion G. M. (2001) Carbonate mineral solubility at low temperatures in the Na–K–Mg–Ca–H–Cl–SO_4–OH–HCO_3–CO_3–CO_2–H_2O system. *Geochim. Cosmochim. Acta* **65**, 1883–1896.

Mavromatis V., Pearce C. R., Shirokova L. S., Bundeleva I. A., Pokrovsky O. S., Benezeth P. and Oelkers E. H. (2012) Magnesium isotope fractionation during hydrous magnesium carbonate precipitation with and without cyanobacteria. *Geochim. Cosmochim. Acta* **76**, 161–174.

Mavromatis V., Gautier Q., Bosc O. and Schott J. (2013) Kinetics of Mg partition and Mg stable isotope fractionation during its incorporation in calcite. *Geochim. Cosmochim. Acta* **114**, 188–203.

Millero F., Huang F., Graham T. and Pierrot D. (2007) The dissociation of carbonic acid in NaCl solutions as a function of concentration and temperature. *Geochim. Cosmochim. Acta* **71**, 46–55.

Morales J., Astilleros J. M. and Fernández-Díaz L. (2012) A nanoscopic approach to the kinetics of anhydrite (100) surface growth in the range of temperatures between 60 and 120°C. *Am. Mineral.* **97**, 995–998.

Nielsen A. E. (1984) Electrolyte crystal growth mechanisms. *J. Cryst. Growth* **67**, 289–310.

Northup E., Kathleen H. and Lavoie D. (2001) Geomicrobiology of caves: a review. *Geomicrobiol. J.* **18**, 199–222.

Palmer D. A. and Wesolowski D. J. (1997) Potentiometric measurements of the first hydrolysis quotient of magnesium

(II) to 250 °C and 5 molal ionic strength (NaCl). *J. Solution Chem.* **26**, 217–232.

Park A. H. A. and Fan L. S. (2004) CO_2 mineral sequestration: physically activated dissolution of serpentine and pH swing process. *Chem. Eng. Sci.* **59**, 5241–5247.

Parkhurst D. L. and Appelo C. A. J. (1999) User's guide to PHREEQC (version 2): a computer program for speciation, batch-reaction, one-dimensional transport, and inverse geochemical calculations. *US Geol. Survey Water Resour. Invest. Rep.* **99**, 312.

Piana S., Jones F. and Gale J. D. (2006) Assisted desolvation as a key kinetic step for crystal growth. *J. Am. Chem. Soc.* **128**, 13568–13574.

Pokrovsky O. S. and Schott J. (2002) Surface chemistry and dissolution kinetics of divalent metal carbonates. *Environ. Sci. Technol.* **36**, 426–432.

Power I. M., Wilson S. A., Thom J. M., Dipple G. M. and Southam G. (2007) Biologically induced mineralization of dypingite by cyanobacteria from an alkaline wetland near Atlin, British Columbia, Canada. *Geochem. Trans.* **8**, 13.

Power I. M., Wilson S. A., Thom J. M., Dipple G. M., Gabites J. E. and Southam G. (2009) The hydromagnesite playas of Atlin, British Columbia, Canada: a biogeochemical model for CO_2 sequestration. *Chem. Geol.* **260**, 286–300.

Pronost J., Beaudoin G., Tremblay J., Larachi F., Duchesne J., Hébert R. and Constantin M. (2011) Carbon sequestration kinetic and storage capacity of ultramafic mining waste. *Environ. Sci. Technol.* **45**, 9413–9420.

Renault R. W. and Stead D. (1990) Recent magnesite-hydromagnesite sedimentation in playa basins of the cariboo plateau, British Columbia. *Geol. Fieldwork Br. Columbia Geol. Survey*, 279–288.

Robie R. A. and Hemingway B. S. (1995) Thermodynamic properties of minerals and related substances at 298.15 K and 1 bar (10^5 Pascals) pressure and at higher temperatures. *US Geol. Survey Bull.* **2131**.

Romanek C. S., Jiménez-López C., Navarro A. R., Sánchez-Román M., Sahai N. and Coleman M. (2009) Inorganic synthesis of Fe–Ca–Mg carbonates at low temperature. *Geochim. Cosmochim. Acta* **73**, 5361–5376.

Russell M. J., Ingham J. K., Zedef V., Maktav D., Sunar F., Hall A. J. and Fallick A. E. (1999) Search for signs of ancient life on Mars: expectations from hydromagnesite microbialites, Salda Lake, Turkey.. *J. Geol. Soc.* **156**, 869.

Saldi G. D., Jordan G., Schott J. and Oelkers E. H. (2009) Magnesite growth rates as a function of temperature and saturation state. *Geochim. Cosmochim. Acta* **73**, 5646–5657.

Saldi G. D., Schott J., Pokrovsky O. S., Gautier Q. and Oelkers E. H. (2012) An experimental study of magnesite precipitation rates at neutral to alkaline conditions and 100–200 °C as a function of pH, aqueous solution composition and chemical affinity. *Geochim. Cosmochim. Acta* **83**, 93–109.

Sawada Y., Uematsu K., Mizutani N. and Kato M. (1978) Thermal decomposition of hydromagnesite $4MgCO_3$–$Mg(OH)_2$–$4H_2O$ under different partial pressures of carbon dioxide. *Thermochim. Acta* **27**, 45–59.

Sayles F. L. and Fyfe W. S. (1973) The crystallization of magnesite from aqueous solution. *Geochim. Cosmochim. Acta* **37**, 87–99.

Schaef H. T., Windisch C. F., McGrail B. P., Martin P. F. and Rosso K. M. (2011) Brucite [$Mg(OH_2)$] carbonation in wet supercritical CO_2: An in situ high pressure X-ray diffraction study. *Geochim. Cosmochim. Acta* **75**, 7458–7471.

Schaef H. T., McGrail B. P., Loring J. S., Bowden M. E., Arey B. W. and Rosso K. M. (2013) Forsterite [Mg_2SiO_4] carbonation in wet supercritical CO_2: An in situ high pressure X-ray diffraction study. *Environ. Sci. Technol.* **45**, 6204–6210.

Schott J., Pokrovsky O. S. and Oelkers E. H. (2009) The link between mineral dissolution/precipitation kinetics and solution chemistry. *Rev. Mineral. Geochem.* **70**, 207–258.

Schott J., Oelkers E. H., Bénézeth P., Goddéris Y. and François L. (2012) Can accurate kinetic laws be created to describe mineral weathering? *C. R. Géosci.* **344**, 568–585.

Shiraki R. and Brantley S. L. (1995) Kinetics of near-equilibrium calcite precipitation at 100°C: An evaluation of elementary reaction-based and affinity-based rate laws. *Geochim. Cosmochim. Acta* **59**, 1457–1471.

Shirokova L. S., Mavromatis V., Bundeleva I. A., Pokrovsky O. S., Bénézeth P., Gérard E., Pearce C. R. and Oelkers E. H. (2013) Using Mg isotopes to trace cyanobacterially mediated magnesium carbonate precipitation in alkaline lakes. *Aquat. Geochem.* **19**, 1–24.

Shock E. L. and Helgeson H. C. (1988) Calculation of the thermodynamic and transport properties of aqueous species at high pressures and temperatures: Correlation algorithms for ionic species and equation of state predictions to 5 kbar and 1000 °C. *Geochim. Cosmochim. Acta* **52**, 2009–2036.

Teir S., Kuusik R., Fogelholm C.-J. and Zevenhoven R. (2007) Production of magnesium carbonates from serpentinite for long-term storage of CO_2. *Int. J. Miner. Process.* **85**, 1–15.

Teir S., Eloneva S., Fogelholm C.-J. and Zevenhoven R. (2009) Fixation of carbon dioxide by producing hydromagnesite from serpentinite. *Appl. Energy* **86**, 214–218.

Temkin M. I. (1963) The kinetics of stationary reactions. *Akad. Nauk SSR Doklady* **152**, 782–785.

Teng H. H., Dove P. M. and De Yoreo J. J. (2000) Kinetics of calcite growth: surface processes and relationships to macroscopic rate laws. *Geochim. Cosmochim. Acta* **64**, 2255–2266.

Thompson J. B. and Ferris F. G. (1990) Cyanobacterial precipitation of gypsum, calcite, and magnesite from natural alkaline lake water. *Geology* **18**, 995–998.

Thrailkill J. (1971) Carbonate deposition in Carlsbad Caverns. *J. Geol.* **79**, 683–695.

Usdowski E. (1989) Synthesis of dolomite and magnesite at 60 °C in the system Ca^{2+}–Mg^{2+}–CO_3^{2-}–Cl_2^{2-}–H_2O. *Naturwissenschaften* **76**, 374–375.

Von Der Borch C. (1965) The distribution and preliminary geochemistry of modem carbonate sediments of the Coorong area, South Australia. *Geochim. Cosmochim. Acta* **29**, 781–799.

Wagman, D. D., Evans, W. H., Parker, V. B., Schumm, R. H., Halow, I., Bailey, S. M., Churney, K. L. and Buttall, R. L. (1982). The NBS tables of chemical thermodynamic properties. Selected values forinorganic and C1 and C2 organic substances in SI units. Journal of Physical Chemistry Reference Data, 11(Suppl. 2), 392.

Walter M. R., Golubic S. and Preiss W. V. (1973) Recent stromatolites from hydromagnesite and aragonite depositing lakes near the Coorong Lagoon, South Australia. *J. Sediment. Res.* **43**, 1021–1030.

Wang J. and Li Z. (2012) Crystallization and agglomeration kinetics of hydromagnesite in the reactive system $MgCl_2$–Na_2CO_3–NaOH–H_2O. *Ind. Eng. Chem. Res.* **51**, 7874–7883.

Wang Y., Li Z. and Demopoulos G. P. (2008) Controlled precipitation of nesquehonite ($MgCO_3{\cdot}3H_2O$) by the reaction of $MgCl_2$ with $(NH_4)_2CO_3$. *J. Cryst. Growth* **310**, 1220–1227.

Wilson S. A., Dipple G. M., Power I. M., Thom J. M., Anderson R. G., Raudsepp M., Gabites J. E. and Southam G. (2009) Carbon dioxide fixation within mine wastes of ultramafic-hosted ore deposits: examples from the Clinton Creek and Cassiar chrysotile deposits, Canada.. *Econ. Geol* **104**, 95–112.

Xiong Y. (2011) Experimental determination of solubility constant of hydromagnesite (5424) in NaCl solutions up to 4.4 M at room temperature. *Chem. Geol.* **284**, 262–269.

Xiong Y. and Lord A. S. (2008) Experimental investigations of the reaction path in the $MgO–CO_2–H_2O$ system in solutions with various ionic strengths, and their applications to nuclear waste isolation. *Appl. Geochem.* **23**, 1634–1659.

Zhang, P. -C., Anderson, H. L., Kelly, J. W., Krumhansl, J. L., and Papenguth, H.W. (2000) Kinetics and Mechanisms of Formation of Magnesite from Hydromagnesite in Brine. Technical Report SAN099 – 1946J. Sandia National Laboratories, Albuquerque, New Mexico, USA.

Zhao L., Sang L., Chen J., Ji J. and Teng H. H. (2009) Aqueous carbonation of natural brucite: relevance to CO_2 sequestration. *Environ. Sci. Technol.* **44**, 406–411.

Associate editor: Chen Zhu